Università degli Studi di Firenze
Scuola di Ingegneria
DIEF - Department of Industrial Engineering of Florence

PhD School: *Energetica e Tecnologie Industriali ed Ambientali Innovative*
Scientific Area: ING-IND/08 - *Macchine a fluido*

Experimental investigation of novel gas turbine combustion concepts operating with CO_2 vitiated air

PhD Candidate: Ing. Giulia Babazzi

Tutor: Prof. Ing. Bruno Facchini

Co-Tutor: Prof. Ing. Antonio Andreini

PhD School Coordinator: Prof. Ing. Giovanni Ferrara

XXXV PhD School Cycle - 2019-2022

It's our choices, Harry, that show what we truly are,
far more than our abilities
- J. K. Rowling

Sentiti libera di diventare quello che vuoi.
Libera di rasarti i capelli a zero,
libera di vestirti come ti pare.
Libera di parlare, guardando dritto negli occhi,
di piangere, di ridere a squarciagola.
Sentiti libera di viaggiare da sola.
Non avere mai paura di sporcarti le mani.
Di asciugarti il sudore.
Lanciati, tuffati, lotta.
Tu puoi fare tutto questo, e molto di più.
Il senso della vita è scritto nei tuoi geni.
- Micaela Miljian Savoldelli

To my family...

Acknowledgements

I've never thought I would do a PhD, actually it was the last thing I wanted to do when I came back from my period abroad to finish my master. But, here I am, after three long years finally ending this journey, after an especially tricky last year. At that moment, it seemed quite a leap of faith, accepting to start a completely new activity: a new test rig, optical windows, reactive conditions, new experimental techniques, new instrumentations...I didn't even know what I was doing, probably that's the reason I accepted and I am happy I changed my mind. So, coming towards the end of this challenging journey, there are quite a few people that I've met along the path that I would like to thank.

First of all I would like to thank Prof. Bruno Facchini and Prof. Antonio Andreini for giving me this incredible opportunity, that made me grow professionally and personally. I also want to thank all the people that works and worked in the HTC group during these years.

A special thanks goes to the THT Lab guys, particularly to Ale and Ricca for their constant help and mentorship. I feel extremely lucky to have had the possibility to face all the challenges with you, I couldn't have asked for better. Mostly, I would like to thank Sofia, my lab mate, for her constant support and for all the funny moments. It wouldn't have been the same without you. I'm sure that Ale and Ricca will miss a lot our noise and chaos during tests.

I wish to sincerely thank Matteo for all the time he spent answering my questions and for every thoughtful discussion, even now that we're colleague. Thanks for the all the laughs at the office, there is a special

inscription for you in the first few lines of the first chapter. Thanks also to my new Baker Hughes colleagues of the Combustion team, for the warm welcome and your support in this first year at the office/last year of PhD. Special thanks goes to Christian for his help in the rig instrumentation phase.

I also wish to thank my friends Le Boscatrici, we've been there for each other since high school and I hope it will always be like that. A special thanks goes to my best friend Luci, who always stands by me no matter what.

Thanks as well to all my friends at the stable, horses included since you've been the best therapy (not cheapest) during these years. Eris as well, I know that you're happier now. Special thanks go to my horse riding instructor and friend Bernardo, for always being there to listen and help me. It meant and still means a lot.

I would also like to thank the person that has recently come into my life, you've helped me more than you could possibly imagine these last few months. Thanks for your care and patience, your presence kept me motivated till the end of this journey.

Finally, I want to thank my family, Grace included, for their constant support even if half of the time they don't even know what I'm talking about. A few lines will never be enough, I just feel so lucky to have you.

Abstract

In the upcoming years, the continuous growth in energy demand will push the energy productions towards more sustainable and efficient solutions. Future stringent regulations and the technologies adopted will drive the greenhouse gases emissions abatement and limit the negative effect on climate change.

While the employment of Exhaust Gas Recirculation (EGR) is a well-established technique in Internal Combustion Engines to limit NO_x emissions, its adoption in Gas Turbine engines has not yet found a practical application due to its expensive and complex installation that hardly ever justifies the emissions reduction when compared to already established Dry Low NO_x combustion technologies. EGR becomes an interesting option in gas turbine engines considering the possibility of increasing the CO_2 content of the exhaust gases to improve the efficiency of Carbon Capture and Storage (CCS) units. However, the decrease in oxygen content of the combustion air is extremely challenging in terms of combustion stability and therefore of engine operability.

In the present work, a novel lean premixed burner for industrial gas turbine applications was studied at ambient pressure in a reactive single-cup test rig. The burner was fed with methane and first characterised in standard air conditions in terms of emissions and stability limits at different operating conditions. The flame position and shape were studied through OH* chemiluminescence imaging, while the burner flow field was analysed thanks to PIV measurements.

The effects of CO_2 addition on the flame were then investigated at

different oxidant oxygen molar fraction decreasing levels, highlighting the impact of the oxygen content on the combustion reaction intensity. Variations in emissions and burner stability limits in terms of maximum sustainable CO_2 content were also studied, to detail the burner operating windows.

The collected data have been thoroughly analysed to gather information on the burner behaviour to support the design of new technical solutions capable of ensuring both proper flame stability and low CO and NO_x emissions. The present work provide a significant contribution to a better understanding of the driving phenomena, proving the importance of dedicated experimental investigations throughout the burner design process.

Contents

List of Figures

List of Tables

Nomenclature

Acronyms

AA	Axial Air
AF	Axial Fuel
C	Convection
CCD	Charge-Coupled Device
CCS	Carbon Capture and Storage
CCU	Carbon Capture and Utilisation
CFD	Computational Fluid Dynamics
CMOS	Complementary Metal-Oxide Semiconductor
DLN	Dry Low NO_x
EGR	Exhaust Gas Recirculation
FEM	Finite Element Method
FoV	Field of View
IRZ	Inner Recirculation Zone
ISL	Inner Shear Layer
K	Conduction
LBO	Lean Blow Out
MCP	Micro-Channel Plate
NGCC	Natural Gas Combined Cycle
ORZ	Outer Recirculation Zone
OSL	Outer Shear Layer

PIV	Particle Image Velocimetry
R	Radiation
RA	Radial Air
RF	Radial Fuel
RMS	Root Mean Square
SL	Shear Layer
TKE	Turbulent Kinetic Energy
VB	Vortex Breakdown

Latin Symbols

A_{an}	Annulus cross-sectional flow area	$[m^2]$
A_c	Surface area of the casing wall	$[m^2]$
A_L	Liner cross-sectional flow area	$[m^2]$
A_w	Surface area of the liner wall	$[m^2]$
d	Diameter	$[m]$
Da	Damköhler number	
D_{an}	Annulus hydraulic diameter	$[m]$
D_L	Liner diameter	$[m]$
k_a	Air thermal conductivity	$[W/mK]$
k_g	Gas thermal conductivity	$[W/mK]$
m_a	Air mass flow rate	$[kg/s]$
m_g	Gas mass flow rate	$[kg/s]$
P_i	Combustor air inlet pressure	$[Pa]$
St	Stokes number	$[-]$
T_3	Coolant temperature	$[K]$
T_{flame}	Flame temperature	[-]
T_g	Gas temperature	$[K]$
T_i	Combustor air inlet temperature	$[^\circ C]$
T_{w1}	Surface temperature of the liner facing the hot gas	$[K]$
T_{w2}	Surface temperature of the liner facing the coolant	$[K]$
U	Axial velocity	$[m/s]$

v	Velocity	$[m/s]$
$\bar{v}$	Time-averaged velocity	$[m/s]$
v'	Velocity fluctuating component	$[m/s]$

Greek Symbols

ε_c	Casing wall emissivity	$[-]$
ε_g	Gas emissivity	$[-]$
ε_w	Liner wall emissivity	$[-]$
μ	Dynamic viscosity	$[Pa \cdot s]$
μ_a	Air dynamic viscosity	$[Pa \cdot s]$
μ_g	Gas dynamic viscosity	$[Pa \cdot s]$
ρ	Density	$[kg/m^3]$
σ	Stefan-Boltzmann constant	$[W/m^2K^4]$
τ	Time	$[s]$

Chapter 1

Introduction

As the world faces the so-called "energy trilemma" of achieving energy security, affordability and sustainability, it is clear that research plays a fundamental role. The continuous growth in energy demand will push the energy production towards more sustainable, flexible and highly efficient solutions. In the upcoming years, the countermeasures and the technologies adopted will drive the greenhouse gases emission abatement and limit the negative effect on climate change. An increasing share of the total amount of energy is produced through renewable sources, well known for their non-programmable and highly fluctuating characteristics. Therefore, the energy sector not only needs to further increase the renewable sources contribution to the total mix but also to address the carbon footprint reduction linked to conventional technologies, based on the use of natural gas and employed to complement and compensate the renewable resources irregular availability.

Looking at the latest International Energy Agency World Energy Outlook [1], even though electricity demand increased by 25% over the last decade, the global CO_2 emissions from electricity generation only rose by 9%. Nevertheless, the electricity sector was responsible for 36% of all energy-related CO_2 emissions. In particular, natural gas is the second largest source of both electricity and CO_2 emissions after coal.

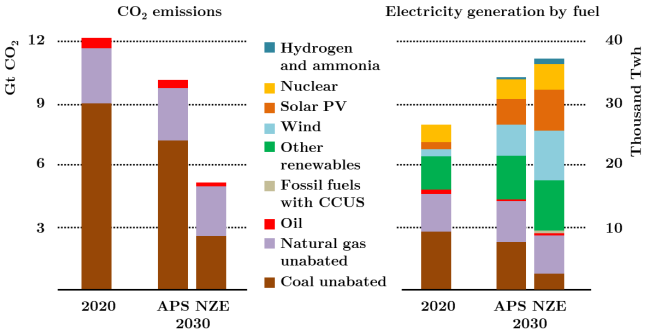

Figure 1.1: Global electricity sector CO_2 emissions and generation by source in the Announced Pledges and Net Zero Emissions by 2050 scenarios [1]

Natural gas employment in the energy sector is supposed to increase from 5% to 15% by 2030, thanks to its essential system flexibility. In advanced economies, it represents the largest source of electricity and its share is going to remain stable over the next decade despite the emerging renewable sources. Therefore, increasing the use of Carbon Capture and Utilisation (CCU) and Carbon Capture and Storage (CCS) technologies is of fundamental importance to reduce greenhouse gases emissions and the cost associated with the decarbonisation.

In order to reduce the cost associated with the CCS implementation and to create an efficient system, the CO_2 content at the inlet of the carbon capture unit must be maximised through the adoption of high percentages of Exhaust Gas Recirculation (EGR). An efficient coupling between the gas turbine system and the CO_2 capture devices is the key to achieve an important power plant emission reduction. On the other hand, such operating conditions push conventional combustion systems to the limit since the oxygen depletion causes a reduction in the combustor operability range.

The EGR employment as a mean to control the flame temperature

and limit NO_x emissions is a common practice in internal combustion engines. However, due to the high costs and complexities related to its installation, it hasn't been considered for real applications to gas turbine engines. Indeed, the achievable reduction in NO_x emissions doesn't justify the power plant complication, especially if compared to the performance of modern Dry Low NO_x (DLN) combustion technologies which are usually able to provide close to single digit emissions [6]. Thus, the most interesting EGR application to gas turbines is related to the achievable increase of CO_2 content in the exhaust gases which would benefit the CO_2 sequestration both in terms of costs and efficiency.

Figure 1.2 shows the schematic representation of a standard Natural Gas Combined Cycle (NGCC) integrated with advanced EGR combustion and carbon capture system. The increase in CO_2 content of the flue gases and the reduction of the volume of the flow entail a radical reduction in CCU/CCS costs and units' size. However, its direct conventional application to gas turbine engines is extremely challenging due to the high volumes involved.

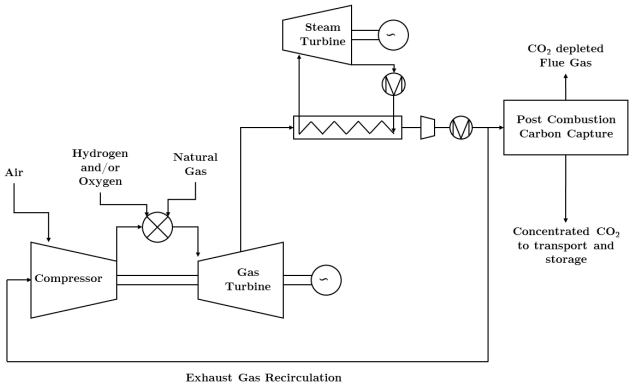

Figure 1.2: Standard scheme of Natural Gas Combined Cycle system (NGCC) integrated with advanced EGR combustion and carbon capture systems [2]

Project Context

Dry Low NO_x combustion technology represents the state of the art gas turbine combustor systems, where lean premixed flames are employed to control the flame temperatures and consequently NO_x emissions [7]. Over the years, several industries have investigated the possibility of combining EGR with lean premixed flames in order to ensure the proper flame stability together with low CO/UHC (unburnt hydrocarbons) and NO_x emissions.

In terms of NO_x emissions, EGR showed promising results. At constant flame temperature and high pressures, the EGR NO_x reduction potential increases as the amount of recirculating gas rises [8]. In addition, compared to standard air cases, the NO_x emissions reduction is even bigger at increasing flame temperatures [9]. The reason behind this behaviour is related to the driving NO_x formation mechanism: EGR NO_x potential reduction is associated to the Zeldovich NO_x formation pathway, thus the reduction is effective only if this is the dominant formation mechanism, so at high pressure and high temperature conditions [10]. This aspect was additionally investigated by several authors that not only confirmed this behaviour but also found an inversion in the NO_x trend for extremely high EGR levels [11]. This trend inversion phenomenon was also investigated through numerical simulations by Burnes et al. [12], who found a threshold in terms of oxygen content of the incoming air above which the NO_x emissions starts rising again.

The real limiting factor associated with the EGR employment is related to CO emissions [13]. The oxygen depletion caused by an increased EGR level drifts the thermodynamic equilibrium towards the CO production. Nevertheless, the CO emissions linked to the equilibrium conditions are only a theoretical value, which is expected to deviate noticeably as the lack of oxygen in the fresh mixture increases [8]. Additionally, the increase in CO emissions is supposed to be particularly pronounced at low loads engine operating conditions, where the lack of oxygen effect overlaps with a decrease in pressure and a significantly lower oxidiser temperature.

As mentioned before, another trivial aspect is the oxygen depletion effect on the flame stability that often leads to the flame extinction. Different strategies have been explored in order to extend the combustor operability window: the majority of researchers studied the employment of a small pilot flame to increase the flame stability at high EGR content [13, 14], while others explored the possibility of employing staged combustion [8, 9].

The EGR impact on the combustion process has been mainly investigated employing numerical methods, most of which are usually limited to low fidelity approaches such as simple one-dimensional studies [15–17] or Reynolds Average Navier Stokes (RANS) simulations [18–21]. Although Large Eddy Simulations (LES) would be preferable in such conditions to provide a detailed understanding of the interaction between the turbulent flow field and the flame characteristics, the available applications are limited to simple combustor configurations due to the modelling high computational costs [22–25].

Despite the significant improvements in terms of computational models and associated costs, their ability to reliably predict the behaviour of complex combustion process and geometries is still limited. Therefore, dedicated experimental investigations are required throughout the design process. In this context, combustion optical diagnostics have been successfully employed in the development and validation of various computational models, allowing a direct visual inspection of the flame and a detailed analysis of the combustion process.

Among the various combustion diagnostics techniques, chemiluminescence bears the potential for an attainable flame diagnostics at various conditions being relatively cheap and easy to implement. This technique is based on the analysis of the electromagnetic radiation emissions naturally released by the chemical species excited during the combustion process. Therefore, the chemiluminescence light carries the information related to the flame local conditions. These aspects make chemiluminescence one of the most attractive techniques in providing detailed results on the behaviour of the reactive process [26].

However, testing at close-to-engine conditions is highly expensive and really challenging, especially when optical diagnostics techniques are involved. Often, at high pressure conditions, optical endoscopes are employed to monitor the flame which do not provide any detail on the combustion process useful for the computational models optimisation [27]. A limited number of available studies investigated at atmospheric pressure the effects of CO_2 addition on the flame behaviour through chemiluminescence measurements, yet considering simple burner geometries [28, 29].

The main objective of this project is therefore to contribute to the development of new burner concepts, able to efficiently operate in alternative operating conditions such as exhaust gas recirculation. Specifically, optical diagnostics measurements will be performed on an industrial burner at ambient pressure conditions to highlight the complexities encountered in the operation of real hardware components. The burner will be tested both in standard air conditions and CO_2 enriched mixtures, to simulate the air vitiation and EGR like conditions. Naturally, recreating real EGR conditions in lab scale is quite challenging because of the associated costs and the volumes involved; the same complications need to be faced when employing N_2 enriched mixtures. Therefore, even if the addition of CO_2 does not exactly match real EGR conditions, such mixtures are considered as a good trade off during the design and primary investigation phases.

The measurements will be used to study the involved combustion phenomena and the complications related to the combustor operability in vitiated air conditions, identifying the limitations of the current technologies and testing the burner ability to adapt to extreme operating conditions. In addition, the collected information represent an important database to be employed for CFD codes validation.

Thesis Structure

The work carried out in this project is divided into two main parts.

A great effort was put in the initial test article development and

experimental techniques implementation, as testing in reactive conditions is extremely challenging. The second part focuses on the presentation of the obtained results.

The dissertation is arranged in the following chapters:

- Chapter 2. This chapter describes the facility at which the experiments were carried out. Then, the test article design is presented together with an explanation of the dedicated instrumentation. Finally, the industrial burner geometry is presented and the rig operating conditions are outlined

- Chapter 3. In this chapter the adopted measurement techniques are thoroughly described. First the Particle Image Velocimetry (PIV) technique is presented, then the OH* chemiluminescence imaging is outlined. For both techniques, an initial part covers the theoretical background while in the final part the measurement layout is provided, together with a detailed explanation of the instrumentation involved that was appropriately selected for this application

- Chapter 4. The results of the PIV measurements are presented and the burner mean flow field is described in this chapter. The PIV measurements were performed both in non reactive and reactive conditions. In addition, the flow field is analysed in terms of root mean square and turbulent kinetic energy.

- Chapter 5. The burner characterisation in standard air conditions is provided in this chapter. Thanks to the OH* chemiluminescence measurements, the flame behaviour is studied at different flame temperatures and fuel split configurations. Pollutant emissions are monitored as well at the tested conditions. The definition of the burner stability limits concludes this chapter.

- Chapter 6. This chapter covers the flame study in vitiated air conditions. The burner is operated at different CO_2-air mixtures, defining the burner operability limits in terms of CO_2 addition. The flame

shape is monitored through OH* chemiluminescence measurements for the tested mixtures, along with pollutant emissions.

The last chapter summarises the main achievements and present the dissertation conclusions, together with recommendations for future work.

Chapter 2

Test Article Design

Contents

This chapter covers the design of the test article, specifically built to test gas turbine burners in reactive conditions at atmospheric pressure. The test article was created to fit inside the reactive test cell of the THT Lab of the University of Florence and to mainly carry out combustion diagnostics investigations. In the following sections the test article design procedure will be illustrated, together with the description of its control system and instrumentation. The investigated burner will be also presented, concluding the rig overview.

2.1 Test rig facility

The test article is integrated in the reactive test cell of the THT Lab of the University of Florence and its schematic layout is outlined in Figure 2.1.

Two screw compressors provide compressed air to the test cell at a maximum pressure of 10 barA, delivering maximum 1 kg/s of mass flow rate. A modulating valve is also integrated in the system to ensure a constant delivery pressure. After the compression, the air flows through various filters and an air dryer (dew point -20 °C) in order to eliminate any impurity and humidity before entering the test cell. Right after, a 600 kW electric heater heats up the air flow at a maximum temperature of 400 °C. In order to keep a constant delivery temperature, a proportional integral derivative system automatically controls the electric heater modulating its power input.

The air mass flow rate is controlled through a globe valve upstream the electric heater, while the rig downstream pressure is set acting on a high temperature control disk valve. A water jacket exhaust duct is placed right after the rig to avoid any interference the back-pressure valve might have on the combustion process. The water jacket is a 1 m long straight duct with circular cross section equipped with four water sprayers, used to quench the hot gases and control the flow exit temperature to keep it in the valve allowable working range. The water system is controlled by dedicated pumps, whose flow rate is set depending on the exhaust gas temperature and the water temperature at the sprayers exit as feedback signal. The air mass flow rate is measured through calibrated orifice flow-meters (standard EN ISO 5167-1), with an absolute uncertainty of 1% calculated following the Kline and McClintock method [30].

The CO_2 employed for the tests in vitiated air conditions is stored in a pressurised tank of about 6000 litres storage capacity. From the storage tank, the CO_2 line directly enters the main air flow line upstream the electric heater, in order to deliver to the test section an homogeneous mixture, both in terms of temperature and composition. The amount of injected CO_2 is controlled through a dedicated valve and measured by a calibrated orifice flow-meter.

As for the fuel line, the test cell is equipped with three natural gas lines that deliver a maximum flow rate of about 90 Nm^3/h. The natural gas directly coming from the local gas network is pressurised from 20 mbar to

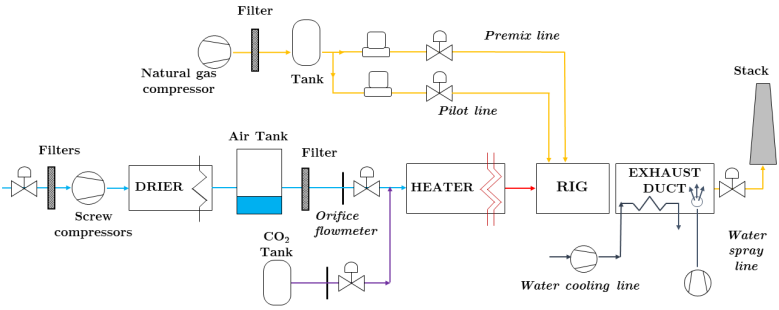

Figure 2.1: Combustion test cell sketch

about 16 bar through a dedicated screw compressor, equipped with special filters to clean the gas from possible impurities. In order to maintain a constant delivery pressure, the compression system automatically adjusts the electric motor rotational speed and the bypass valve aperture. A 200 litres tank is also present along the delivery line to smooth out any pressure fluctuation. Each fuel line is provided with a globe valve to control the flow rate and a shut off valve for safety reasons, together with a Pt100 resistance temperature detector probe, pressure gauges, and a specific mass flow meter.

2.2 Test article design and dedicated instrumentation

The test article was designed in order to be integrated inside the reactive test cell of the THT Lab of the University of Florence, thoroughly described in the previous section. It was conceived to allow optical measurements on the flame region and it is characterised by a modular layout to adjust the system to different burner concepts changing only a limited number of components. The modular design is also necessary to

allow inspection, cleaning and replacement of components. A cross-section of the designed test article is shown in Figure 2.2.

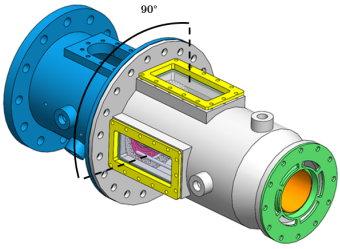

(a)

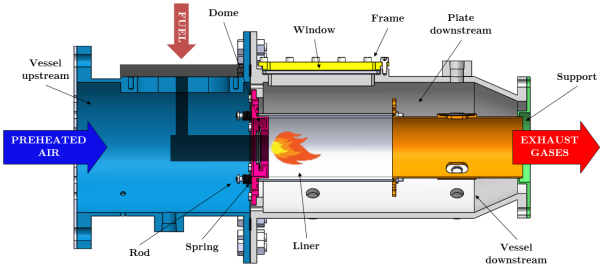

(b)

Figure 2.2: Test article CAD and cross-section

The test article consists of two main parts: the casing, which constitutes the enclosure that confines the air and the reactive process ensuring a safe test operation, and the combustor, which is the flame enclosure system.

In turn, the outer casing is made of the following items:

- The upstream vessel, thanks to which the test article is connected to the lab air supply system. The burner is attached to the test

article through a flange created on the upper surface of the upstream vessel.

- The downstream vessel, which is the component that actually hosts the combustor. On its external surface there are the two seats for the optical windows installation and other accesses for the possible insertion of different measuring probes. The downstream vessel is connected to the downstream lab test rig quenching system.

- Two optical accesses made of quartz windows, held in place by frames connected to the vessel through bolted joints. Graphite gaskets are here employed to avoid the direct contact between the metal and the quartz windows and to avoid any leakage. The windows are disposed at a 90° angle.

The combustion chamber consists of the following components:

- The dome, on which the burner is mounted thanks to a ferrule used to help the burner centering and to ensure a perfect alignment between the burner exit section and the dome surface. Since it is really close to the flame, the dome surface is cooled through a series of radially inclined effusion holes to avoid possible problems that high metal temperatures could cause. The dome is screwed to the downstream vessel and it is shaped to host the liner.

- The plate-downstream, which has different accesses for the possible installation of measuring probes and it is used to convey the exhaust gases towards the test rig exhaust system.

- The liner, made of a quartz cylinder to ensure a proper visibility of the flame region. The tests can be carried out with two different liners, with an internal diameter of 110 mm or 130 mm. Each one of them can be employed individually or they can be used together to ensure a better cooling of the one directly facing the flame. Care must be taken in ensuring a proper temperature gradient across the liner thickness, as the quartz is a particularly delicate material. For

this application a quartz liner of 2.5 mm of thickness was selected. In both configurations, graphite gaskets are employed to avoid a direct contact with the metal surfaces and to ensure an effective sealing.

- The liner blocking system, which consists of four tie rods and four springs that connect the dome to the plate-downstream. The springs are suitably preloaded through nuts screwed on the tie rods to hold the liner in position while always maintaining contact between the components. This was mainly done to avoid any leakage but to allow at the same time the components thermal expansion due to temperature variations.

- A final support, that upholds the plate-downstream. A small gap between the two components was created to avoid any possible blockage effect in the event of thermal expansion.

As mentioned, both the liner and the optical accesses are made of quartz. Inconel 718 was employed to manufacture the dome due to the high temperature exposure, while all other metal parts are made of AISI 304.

The test article design was an iterative process divided into two main steps, one for the air split definition and one for the thermo-structural verification. All the analysis were conducted considering the baseline test article configuration, that is employing the smaller liner.

As for the air-split, the amount of preheated air entering the test section is divided between the flame region and the cooling system. However, for the electric heater to work efficiently and reach the targeted temperature, a minimum amount of mass flow needs to be processed which was therefore taken as the total amount of preheated air at the rig inlet. Once set an average amount of air passing through the burner for the combustion process, the cooling system was designed to drain the remaining amount of air at the nominal operating conditions and ensuring a proper cooling at the same time. About 90% of the incoming air is used to feed the cooling system, while the residual 10% passes through the burner and

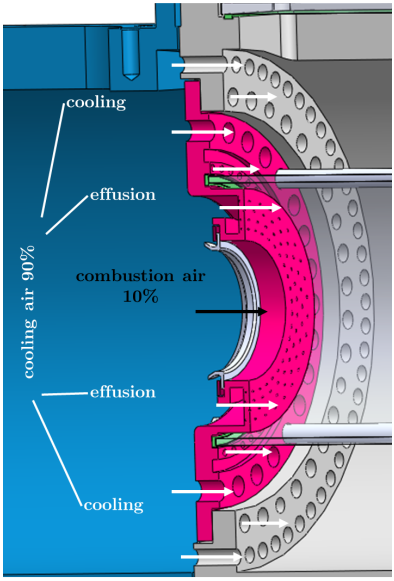

Figure 2.3: Test rig air split scheme in nominal operating conditions

enters the combustion chamber (Fig. 2.3). During the rig commissioning, the actual flow split and the various holes effective areas were verified in fluxing conditions with a know air mass flow rate.

The thermo-structural analysis was carried out through FEM simulations employing Ansys Workbench. Initially, a thermal analysis was used to estimate the temperature distribution on the different components and the deriving thermal field was then imported as load in the structural analysis.

A simplified thermal analysis is carried out considering the convective (C) and radiative (R) loads from the flame towards the liner (1) and from the liner towards the vessel (2), schematically represented in Figure 2.4. Indeed, the liner is heated by radiation and convection from the combustion products and it is cooled by convection of the cooling air flowing in the annulus and by radiation towards the casing. The amount of heat transferred depends mainly on the geometry and on the combustor operating conditions. Once the equilibrium conditions are reached, the liner reaches a temperature such that the internal and external heat fluxes are balanced. As for the conduction, the conduction along the liner wall is small compared to the other fluxes and it is usually neglected; therefore, only the conduction across the liner thickness was considered (K). Heat transfer coefficients and bulk temperatures were calculated through Lefebvre equations [31]:

$$R_1 + C_1 = R_2 + C_2 = K_{1-2} \tag{2.1}$$

$$R_1 = 0.5\sigma(1+\varepsilon_w)\varepsilon_g {T_g}^{1.5}({T_g}^{2.5} - {T_{w1}}^{2.5}) \tag{2.2}$$

$$C_1 = 0.02\frac{k_g}{D_L^{0.2}}\left(\frac{m_g}{A_L\mu_g}\right)^{0.8}(T_g - T_{w1}) \tag{2.3}$$

$$R_2 = \sigma\frac{\varepsilon_w\varepsilon_c}{\varepsilon_c + \varepsilon_w(1-\varepsilon_c)(A_w/A_c)}(T_{w2}^4 - T_3^4) \tag{2.4}$$

$$C_2 = 0.02 \frac{k_a}{D_{an}^{0.2}} \left(\frac{m_{an}}{A_{an} \mu_a} \right)^{0.8} (T_{w2} - T_3) \tag{2.5}$$

$$K_{1-2} = \frac{k_w}{t_w} (T_{w1} - T_{w2}) \tag{2.6}$$

where:

- σ is the Stefan - Boltzmann constant
- ε_w is the liner wall emissivity
- ε_g is the gas emissivity
- T_g is the hot gas temperature
- T_{w1} is the surface temperature of the liner side that exchanges heat with the hot gas at temperature T_g
- k_g is the gas thermal conductivity
- D_L is the liner diameter
- m_g is the gas mass flow rate
- A_L is the liner cross sectional flow area
- μ_g is the gas viscosity
- ε_c is the casing wall emissivity
- A_w is the surface area of the liner wall
- A_c is the surface area of the casing wall
- T_3 is the cooling air temperature
- T_{w2} is the surface temperature of the liner side that exchanges heat with the cooling air at temperature T_3
- k_a is the cooling air thermal conductivity

- D_{an} is the annulus hydraulic mean diameter
- m_a is the cooling air mass flow rate
- A_{an} is the annulus cross sectional flow area
- μ_a is the cooling air viscosity

The presented equations were therefore employed to calculate and impose convective and radiative loads to the geometry in the FEM thermal simulation.

As expected, both the dome and the liner are the components that reach the highest temperatures being in direct contact with the flame. However, the obtained temperature distribution remains below the material allowable maximum temperature for both the metal and the quartz.

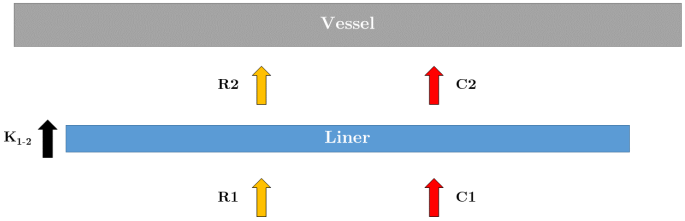

Figure 2.4: Simplified representation of the thermal loads considered in the thermal analysis: C and R are respectively the convective and radiative loads from the flame towards the liner (1) and from the liner towards the vessel (2). K is the conduction across the liner

The resulting temperature distribution was then imposed as load in the structural analysis, together with the static operating pressure, which was set to a higher value than the actual ambient test conditions for safety reasons. The structural results in terms of components mean stress were

therefore analysed in order to verify not to exceed the material maximum allowable stress.

All bolted joints were analysed as well during the structural assessment to ensure a safe operation of the test article. In particular, the joints pre-load was adjusted to not overload the bolts but to guarantee at the same time a proper contact between components.

In addition, both the central flanges to connect the two vessels and the containment vessel design were verified applying the ASME Rules for Construction of Pressure Vessels whose standards were taken as reference [32]. As for the flanges, the regulation provides two different operating conditions, namely "seating" and "operating", in which the following loads are involved:

- HD - Operating. This load is given by the duct attached to the flange

- HT - Operating. The load is created by the internal pressure that acts on the gasket. The pressure acts on the exposed edge of the gaskets which in turns tries to expand. However, the gasket is held in place by the flange faces that squeeze the gasket. In the end, the resulting force that develops between the flange and the gasket will have a triangular distribution (Fig. 2.5), where the force is 0 at the external gasket diameter and reaches its maximum value along the internal edge, that corresponds to the applied internal pressure. Commonly, the HT load is calculated as an average pressure and it is usually applied at an height that corresponds to about 1/3 of the triangular distribution

- HG - Operating. This is the force required to keep the flange sealed against the operating pressure and it is generated by the tightening bolts that connects the two flanges

- HG - Seating. This term represent the force required to hold the gasket in place and to avoid leakages depending on the operating pressure. The HG load calculation is based on the gasket properties.

However, an actual correlation with real properties and their inclusion in structural FEM calculations leads to a significant increase in computational costs. Therefore, this term is not usually considered to predict the flange stress.

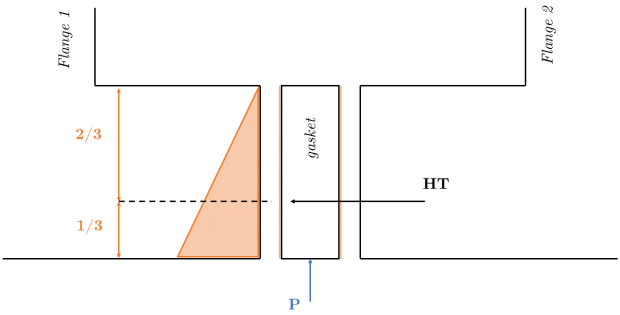

Figure 2.5: Flange HT load schematic representation

Following these standards, the aforementioned loads on the flanges were calculated at the design operating conditions and imposed on the geometry for the structural analysis. An appropriate flange thickness was then selected to guarantee structural safety and a proper sealing.

Particular attention was dedicated to the spring sizing, since they play a major role in the test article design as explained in the previous sections. The spring type and the relative pre-load were chosen taking into account the components weight and their relative thermal expansion, ensuring at all times a minimum applied pressure on the gaskets for an appropriate sealing.

As for the optical components, the quartz cylindrical liner thickness of about 2.5 mm was selected in order to minimise the temperature gradient across the liner thickness. Similarly, the vessel optical accesses were sized according to the design indications for pressurised windows, specifically for rectangular shaped windows in a fixed seat. The windows thickness was chosen in order to guarantee the integrity of the accesses under the

given operating pressure. Even if the vessel was designed to withstand a pressure of about 5 bar, this study focuses on the burner characterisation at ambient pressure and the resulting minimum window thickness for a safe operation corresponds to about 5 mm. However, the rig was designed to host also thicker windows to account for a possible rise in the operating pressure.

Test article instrumentation

Concerning the rig instrumentation, the test article is equipped with various thermocouples and static pressure ports. Two static pressure taps are positioned in the upstream vessel to monitor the flow inlet pressure, one pressure port is placed on the casing to measure the annulus pressure, while two other pressure taps are located in the flame tube downstream the quartz liner (Fig. 2.6 section G). The static pressure is measured employing a NetScannerTM System pressure scanner with temperature compensated piezo-resistive relative pressure sensors.

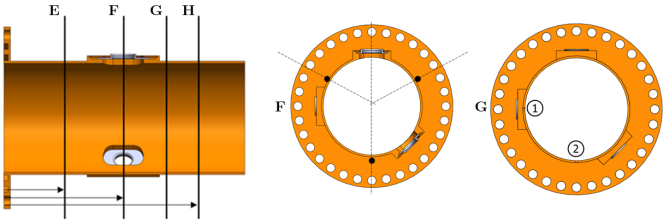

Figure 2.6: Detail of the instrumentation on the plate downstream component: section E-F-H are the thermocouples locations while section G is where the pressure port are located

In addition, both the flow and metal temperatures are monitored in

different locations of the rig. The incoming air temperature is measured through two thermocouples positioned in the upstream inlet chamber, while metal temperatures are acquired to keep under control the rig temperature gradients. Two thermocouples measure the dome surface temperature, while the flame tube thermal behaviour is monitored through 9 K-thermocouples positioned at 3 different axial measurement stations in 3 distinct circumferential locations downstream the quartz liner (Fig. 2.6 section E-F-H). A data acquisition/switch unit HP/Agilent connected to an external reference junction is employed to measure the temperature.

The flame tube is also equipped with a PCB piezotronic probe to continuously monitor pressure fluctuations during the course of each reactive test.

In order to perform tests in reactive conditions, the rig is additionally provided with a spark plug to ignite the mixture, located along the flame tube downstream the optical liner .

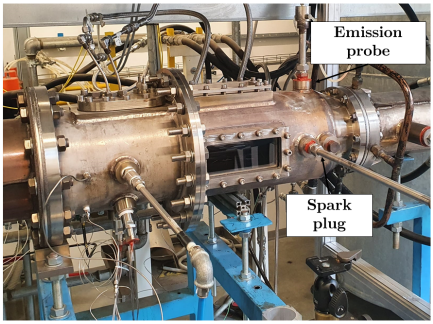

Figure 2.7: Combustion test rig at the THT Lab of the University of Florence

An emission probe is also present, employed to analyse the exhaust composition through a HORIBA PG250. The probe is made of several radially spaced holes and it is plunged into the flame tube to extract the exhaust gases. After being extracted, the gases reach a gas analyser through a thermally insulated 6 mm teflon pipeline that keeps the gas

mixture at a constant temperature of about 150°C. Before reaching the analyser, a HORIBA PS200 refrigerator is used to remove any trace of water vapour from the gas sample. The gas analyser is properly calibrated right before each test employing a rack of calibrated gas mixture tanks.

An in-house LabVIEW software tool is used for real time monitoring of all the principal rig parameters. The acquired data at each test point are obtained by averaging the measured values for 30 seconds, once reached the desired stationary conditions. A picture of the test rig and the relative instrumentation is showed in Figure 2.7.

2.3 Burner description and operating conditions

The investigated burner is a novel lean premixed burner developed by Baker Hughes for industrial gas turbine applications. A thorough description of the burner geometry and its development can be found in the works of Cerutti et al. [33–35].

The burner cross-section is illustrated in Figure 2.8.

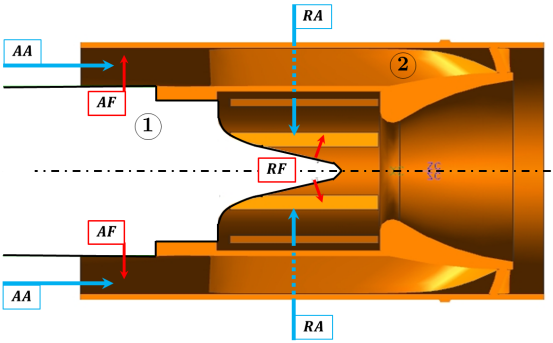

Figure 2.8: Investigated burner architecture

The burner mainly consists of two different parts:

- Part 1 of Figure 2.8 is the fuel injector, equipped with two distinct fuel injection locations

- Pat 2 of Figure 2.8 is the premixer, composed by two independent flow passages. Each one of them provides a different amount of swirl to the air-fuel mixtures

Each one of the fuel injection rows is independently fed and regulated by a different fuel gas line.

According to Figure 2.8 notation, a first air stream AA (Axial Air) enters the burner through an axial swirler and mixes with the first row of axial fuel injectors AF (Axial Fuel) present within the external passage, just upstream the axial swirler, creating a premixed flame. The second air stream RA (Radial Air) flows through the internal radial swirler before mixing with the radial fuel stream RF (Radial Fuel) to feed the internal diffusion flame. The following throat is properly sized to ensure an appropriate mixture acceleration before the downstream sudden section expansion, which corresponds to the flame front developing region. Regardless of the amount of residual flow swirl, the flame stabilisation mechanism is mainly driven by the inner throat size and the law of cross-sectional area increase of the downstream dump region. As pointed out from previous investigations [33–35], the flame stabilisation process is also strongly affected by the amount of overall thermal power released in each region through the dedicated radial and axial fuel injections. The air split between the inner and the outer passages is determined by the passages shape and size, therefore the resulting swirl number is a mass weighted swirl number calculated according to each passage contribution.

The burner was tested in different operating conditions in order to study the flame changes in shape and position through combustion diagnostics techniques. The operating conditions are determined through the following main control parameters:

- T_i is the combustor inlet temperature, set to 300 °C to simulate close to reality compressor discharge temperatures

- P_i is the combustor air inlet pressure. As early mentioned, the test campaign was conducted at ambient pressure

- ΔP is the pressure drop across the combustion chamber, calculated as the differential pressure across the combustor divided by the combustor inlet pressure. The majority of the test was performed at a ΔP of about 4.5% which corresponds to the optimal value for a good flame stability. A few tests were executed at different pressure drops to study its effect on the flame stabilisation

- T_{flame} is the flame temperature, calculated as the adiabatic flame temperature assuming a perfect mixing between the burner combustion air and the total amount of fuel injected. The flame temperature values are scaled with the typical ISO base load flame temperature for proprietary reasons

- the fuel split between the radial and the axial fuel lines, which is expressed as percentage of the total fuel amount per each fuel injection row.

Therefore, these parameters will be used in the following sections to define the tested conditions. If not otherwise specified, the ΔP is kept constant to 4.5% throughout the test campaign.

An additional parameter was used to assess the burner behaviour in close-to EGR conditions: the air vitiation is expressed as oxygen molar concentration (O_2 %), reached after the addition of a certain amount of CO_2 into the main air flow entering the test rig.

Chapter 3

Experimental techniques

Contents

The investigation of the burner behaviour has been carried out mainly through two different experimental techniques, which will be detailed in this chapter. The basic theory behind each of the adopted techniques will be covered, followed by the description of their specific application in the present test campaign.

3.1 Time-resolved PIV

Particle Image Velocimetry (PIV) is an optical measurement technique that allow to measure the velocity field of an extensive region. This is an important and fundamental feature compared to point measurements methods where the flow velocity is measured at a single point employing probes such as hot wires or pressure tubes. Figure 3.1 schematically

depicts a generic set-up for PIV measurements. The PIV technique is based on the introduction of seeding particles in a flow, whose movement is tracked over time to capture the mean flow field. The particles material and dimensions vary depending on the environment in which they need to be inserted: inert substances have to be used to not alter the flow and they need to be small enough to be able to follow the streamlines of the flow field without altering it. A high density energy laser system and a set of optical lenses are used to generate a thin sheet of monochromatic light to illuminate the seeding particles. The particles are usually illuminated twice by a laser sheet and the light scattered by the tracer particles is recorded by means of a CCD (Charge-Coupled Device) camera to track their position. In order to estimate the particle velocities, the acquired images are divided in small interrogation areas assuming that the particles are moving homogeneously within each area and a displacement vector associated to the particle movement is computed using a statistical approach based on 2D cross-correlation methods. The velocity vectors are finally computed directly from the displacement vectors, taking into account the time delay between the pair of images and the magnification factor, derived from the spatial calibration of the imaging system to relate the CCD pixels to physical length.

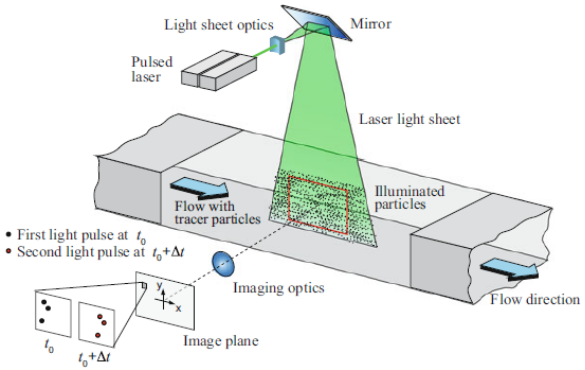

Figure 3.1: A typical layout for 2D-PIV measurements [3]

Therefore, analysing the various instantaneous images, the PIV technique allows to calculate the mean flow field and derive some useful information related to the turbulence level of the flow.

Measurement theory

As mentioned above, the seeding particles diameter have to be small in order to follow the flow field. The Stokes number is a dimensionless number usually used to describe the capability of the particles to follow the mean flow field:

$$St = \frac{\tau U}{d_p} \tag{3.1}$$

where U is the local drag flow velocity, d_p is the particle diameter and τ is the response time of the particle. When the particles Reynolds number is less than unity, the flow is defined as Stokes flow. In Stokes flows, the particle drag coefficient is inversely proportional to the particles Reynolds number and the characteristic time of the particle is defined as:

$$\tau = {d^2}_p \frac{\rho_p}{18\mu} \tag{3.2}$$

This formulation applies as long as the seeding density is much greater than the flow density. In order for the particles to follow the streamlines, the seeding St number should be as low as possible. In particular, for $St > 1$ the particles movements is not associated to flow motion especially in case of abrupt deceleration. On the contrary, for $St << 1$, the particles closely follow the fluid streamlines and if $St << 0.1$ accuracy errors related to tracing usually stay below 1% [36]. As the fluid is in constant acceleration, the particle response time generates a lag in the particle velocity with respect to the real flow velocity. This phenomena generates an exponential trend of the particle velocity (Up) that can be expressed as a function of time as follows:

$$U_p(t) = U\left(1 - exp\left(-\frac{t}{\tau}\right)\right) \tag{3.3}$$

If the acceleration of the flow is not constant or Stokes drag does not apply, like in turbomachinery applications, the particle motion definition becomes more complex. However, τ still represents a good approximation to measure the particles tendency to achieve the equilibrium in terms of velocity with the flow [3].

In addition to the above mentioned characteristics, the seeding particles must have good Mie scattering properties to maximise the scattered light and improve the measurement sensitivity. Normally, either gasous, liquid or solid seedings can be employed depending on the application. The latter is commonly used in case of high temperatures or reactive flow conditions.

3.1.1 PIV measurement set-up and data post processing

The combustion flow field was studied thanks to the rig wide optical accesses. The PIV investigations were carried out employing the Dantec-Dynamics PIV system, where the Dantec-FlowManager ©software was used to control all the instrumentation settings, as well as synchronisation, acquisition and post processing. The laser adopted in this test campaign is the Litron LDY303, a Nd:YAG pulsed laser at a wavelength of 527 nm with a sample rate range between 0.2 and 20 kHz and a power range of 0-20 mJ. The images were recorded through a Phantom MIRO M340 camera, which has a resolution of 2560x1600 pixels and a 12 bit sensor depth. The camera sensor is a 4 mpx CMOS 25.6 mm x 16.0 mm sensor with a 10 μm pixel size. The camera acquisition frequency is of 800 fps at full resolution and it can be increased up to 50 kHz by lowering the camera resolution. The camera was coupled with a Micro NIKKOR 60mm $f/2.8$ lens and a band pass filter to cut out all the incoming light except for the laser light scattered by the seeding particles.

Due to the reactive conditions of the test, titanium dioxides particles (submicron mean size) were used to seed the air flow directly upstream the burner. The particles were injected employing the Lavision Particle Blaster 110. This solid particle seeder is made of a swirling bed generator consisting of a magnetic stirrer and a magnetic bar housed in a cylinder

container. The air flow at the inlet of the seeder can be controlled by adjusting the pressure control valve to increase or decrease the particles density depending on the tested conditions.

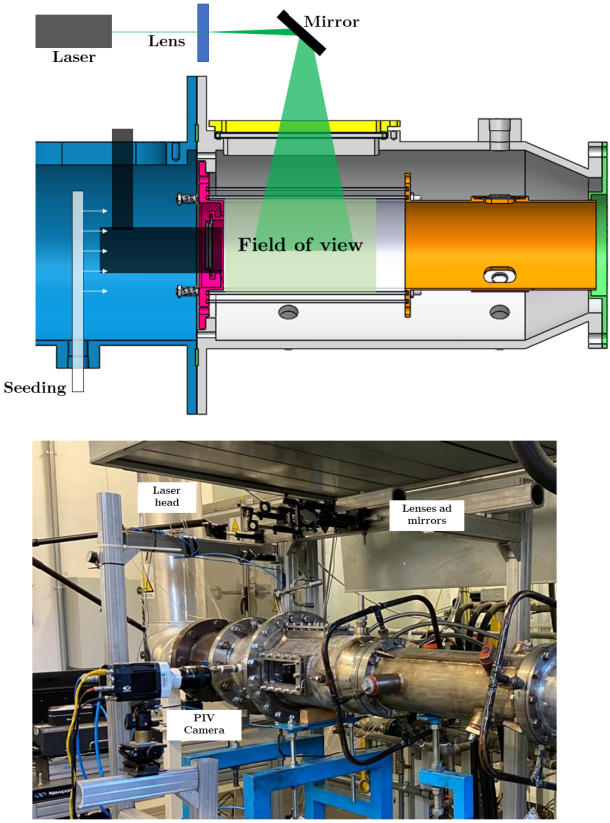

Figure 3.2: PIV system set-up

The PIV set-up used for this test campaign is illustrated in Figure 3.2. The laser beam is shaped into a thin laser sheet thanks to an accurately designed optical trail, made of a series of lenses and a final mirror mounted on an adjustment system to project the laser sheet into the desired portion

of the test rig. As shown in the scheme, thanks to the camera lens and the wide optical accesses of the rig, it was possible to analyse the mean flow field at the central section of the burner with a single Field of View (FoV): the analysed region reaches a distance far from the burner exit of about 2 times the chamber diameter, which is normally assumed as enough for the flow to be fully developed. The flow was seeded employing a multi hole distribution pipe that was positioned right at the back of the burner to ensure good seeding homogeneity. In order to weaken the reflections inside the chamber and to limit the Signal-to-Noise ratio to tolerable values, the vessel was painted in black employing a high temperature resistant paint. For obvious reasons, the cylindrical quartz liner could not be painted. Therefore, this caused the appearance of some strong reflections, that led to an erroneous calculation of the vectors in some confined regions. This issue will be further addressed while presenting the PIV measurements results.

For all the tested conditions, the camera was calibrated employing a calibration dot pattern. The camera was mounted on a portal structure fixed on the same carriage where the test rig was positioned to avoid any possible effect of the thermal expansion on both calibration and measurements. As it will be detailed in the results section, both cold and reactive tests were conducted acquiring images at a frequency of 400 Hz and the time delay between the two laser pulses was varied between 7 and 9 μs. For each tested condition, about 500 pair of images were acquired to assure statistical convergence of the results. Each set of image pairs has been post processed using an adaptive grid iterative approach. This method is an automatic and adaptive method that iteratively adjusts in size and shape the individual interrogation areas to adapt to local flow gradients and calculate the velocity vector. The adaptive PIV method is the most suitable choice to limit the in-plane drop-out particles, as during the time delay between the two laser pulses the particles could leave the interrogation area, reducing the signal strength and the number of valid vectors. To prevent outliers from perturbing the velocity measurements, the vectors were validated applying on the image cross-correlation the

peak validation and the Universal Outlier Detection algorithm, where each rejected vector is substituted with the median of the neighbouring vectors [37]. The thus obtained raw data were then further post processed to extract some useful information of the burner flow field, as it will detailed in the following chapters.

As commonly known, the PIV system is affected by several errors which are mostly difficult to weight and take into account in a sort of uncertainty quantification. Some of the them can derive from the calibration, the camera sensor not perfectly perpendicular to the measurements plane, image distortion due the aberration of the lenses, non-perfect alignment of the laser sources, fluctuations in the laser power, seeding non homogeneity and so on. According to Wersterweel [38], thanks to the sub-pixel interpolation, the uncertainty on the particle displacement calculation should be in the range of 0.1 pixels.

3.2 Chemiluminescence

Chemiluminescence is the radiation that atoms, molecules or radicals emit while returning from an excited electronic state to the ground electronic state. The released energy directly comes from chemical reactions and for this reason it can be found in any process that involves unstable and intermediate species, such as combustion processes. Therefore, the chemiluminescence emission does not need any external excitation and only a camera, specific for this type of light conditions, is necessary to collect data.

The analysis of the chemiluminescence light released by the flame allows to monitor the flame position and its dependence on the operating conditions, which makes this technique suited for diagnostic purposes. Being additionally relatively cheap to implement, it can be therefore used to support the optimisation process of new and existing burner concepts in terms of flame position, material lifetime as well as contribute to the validation of CFD models. While qualitative information about the flame temporal and spatial characteristics variations can be quite

easily gathered, care must be taken when trying to analyse the data quantitatively. Indeed, chemiluminescence is a line-of-sight technique: the emission intensity acquired trough the camera includes the contribution of every molecule that the camera can see, integrated along the ideal line that connects the CCD sensor to the measurement point.

Measurement theory

The radiation wavelength is characteristic of the specific molecule and the particular transition the molecule is undergoing. The more complex is the molecule, the more complex is its radiation spectrum. Figure 3.3 illustrates a typical methane-air flame chemiluminescence spectrum at atmospheric conditions. Generally speaking, spectrum are an overlapping of the emissions coming from different molecules and atoms. In this case, four electronically excited species are recognisable: the broadband molecule $CO^*{}_2$ and the radicals OH*, CH* and $C^*{}_2$, which instead emit light in a narrow band of the spectrum.

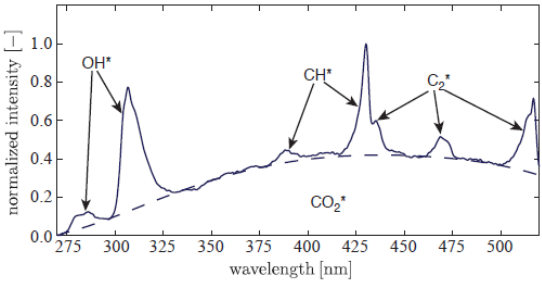

Figure 3.3: Typical chemiluminescence emission spectrum of a methane-air flame at atmospheric conditions [4]

In particular, OH* chemiluminescence is the most studied species in combustion diagnostics as it can be considered as flame heat release marker [26, 39, 40]. Therefore, this research will focus on OH* chemiluminescence to study the flame shape and its position depending on the different operating conditions.

A brief introduction on the fundamentals of chemiluminescence are introduced in this section analysing the radical OH* as it is the main interest of this research, however they could be used to describe any other radical or molecule emission. A full and thorough analysis from a theoretical point of view can be found in [41–43].

Spectral lines in molecular spectroscopy are associated with the absorption, emission and scattering of a proton whenever the energy of a molecule changes. The various energy states correspond to changes in the electronic configurations and nuclei vibrations and rotations. Using the Born-Oppenheimer approximation, the energy of a molecule is given by three different energies: the electronic energy E_{el}, the vibrational energy E_{vib} and the rotational energy E_{rot}:

$$E = E_{el} + E_{vib} + E_{rot} \tag{3.4}$$

Generally, transitions corresponding to changes in the rotational energy level belong to the far infrared and microwave portion of the spectral region, the one happening within the vibrational energy levels belong to the infrared spectral region, while transitions between electronic energy levels are in the visible or ultraviolet portion of the spectrum. Usually, vibrational transitions result in changes in the rotational mode while electronic transitions cause changes in both the rotational and vibrational mode.

The lowest electronic state is the ground electronic state and it is called the X-state. The following states at higher energy are called A-state, B-state and so forth. In each electronic state, the vibrational energy is characterised by the quantum number ν: ν" is the vibrational quantum number of the ground electronic state and ν' is the one of the upper excited electronic state A. As explained before, molecules can also rotate and the rotational energy associated to each vibrational state is identified by the rotational quantum number J: J" is the rotational quantum number of the ground electronic state and J' is the rotational quantum number of the excited A-state. Therefore, various transitions can be possible and they are ruled by specific selection rules that determines if a transition is

allowed.

Figure 3.4 shows a simplified diagram of the energy levels of the OH radical, with the potential curves of the ground electronic state and the first excited electronic state. The potential curves represent the radical energy level as a function of the nuclei distance: when the nuclei are close to each other the energy is very high; as the distance increases, the radical first crosses a stable region with lower energy and then it starts to dissociate into the atoms O and H. For each electronic state, both the potential and the rotational curves with the notation explained before are illustrated. The OH* ground electronic state is usually denoted as $X^2\Pi_i$, while the electron configuration of the first excited electronic state is written as $A^2\Sigma^+$ [5].

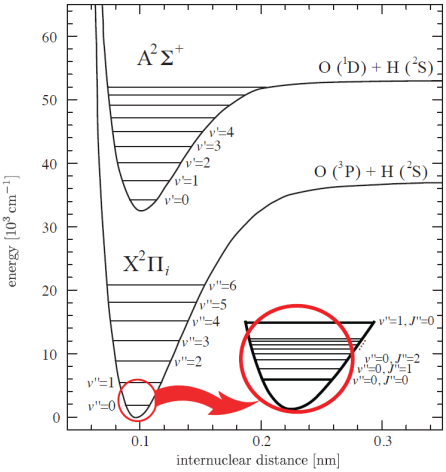

Figure 3.4: Simplified diagram of OH radical energy levels [5]

Generally, excited electronic states are not stable and molecules tends to return to their ground electronic state. This can happen through two possible ways, namely fluorescence and collisional quenching. Fluorescence is the spontaneous emission of a photon containing the energy difference between the two energetic levels. However, the most common

transition to the ground electronic state is through collisional quenching, a deactivation mechanism that transfers energy through collision with a third body and can lead to transition to both higher or lower energy levels. The equilibrium distribution of the excited radicals depends on the ratio between upward and downward transitions and it is a function of temperature. The OH radical spectrum is thus determined by the equilibrium distribution of the rotational and vibrational states and the Einstein coefficients for spontaneous emission, which represents a proportionality factor between the number of excited radicals and the chemiluminescence emission intensity. The chemiluminescence spectrum shows the characteristic band of the different rotational and vibrational transitions and their relative intensity. Specifically, the peak intensity around 309 nm of Figure 3.3 is the OH* strongest emission band and it originates from the transition with $\Delta\nu = 0$. For this reason, this investigation focuses on this transition, denoted as $X^2\Pi_i(\nu" = 0) \leftarrow A^2\Sigma^+(\nu' = 0)$.

3.2.1 Chemiluminescence measurement set-up and post processing

Chemiluminescence measurements of the OH radical were employed to detect the reaction zone and its position in various operating conditions. In order to carry out this type of measurements, an intensified camera or a camera coupled with an image intensifier have to be used. The same camera used for the PIV measurements, the Phantom MIRO M340, was coupled with the Hamamatsu C16031-311-Ax image intensifier through a relay lens. In addition, a Nikon UV 105mm $f/4.5$ lens together with a bandpass filter (CWL = 310 +/- 2nm; FWHM = 10 +/- 2nm) were mounted on the image intensifier to be able to capture the OH* transition mentioned before, which has its peak emission intensity in the UV spectrum. The optics set-up for this test campaign is schematically illustrated in Figure 3.5.

A CCD or CMOS camera needs to be coupled with an image intensifier mainly to enhance the camera sensitivity up to single photon detection and to extend the camera spectral sensitivity for UV radiation detection. An

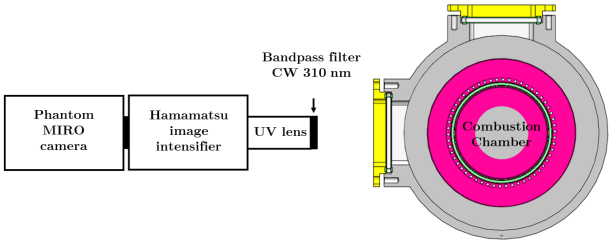

Figure 3.5: Chemiluminescence set-up

image intensifier is a device that boosts the intensity of the incoming light by converting photons to electrons and back to photons. It is essentially made of three components:

- The photocathode is the entrance of the image intensifier and it is the sensitive element of the image intensifier. The photocathode converts the incoming photons into electrons and its material is selected depending on the application. The quantum efficiency of the photocathode specifies the efficiency of this conversion depending on the wavelength. For this application a Multikali photocathode was selected as it covers light emissions in the range 180 - 900 nm, with the highest quantum efficiency in the range 200 - 500 nm.

- The Micro-channel plate (MCP) is the second element of the intensifier and it's where the electrons are multiplied. The MCP is usually a glass plate with millions of tilted channels. The electrons are accelerated thanks to a a variable voltage (gain) and the number of electrons amplifies with each collision on the channel walls. So the higher is the gain, the higher is the number of emitted electrons.

- A phosphor screen which is the output of the image intensifier, where the electrons are transformed back to photons. It is a layer of phosphorescent material that emits light upon electrons impact. Depending on the type of phosphor, the intensity of the emitted light will decrease faster. The more efficient the phosphor, the slower

its light intensity decays after excitation. The two mainly available phosphor screen are the P43 and P46. The chosen phosphor for this study is the P46, whose conversion efficiency is a bit lower than the P43 but it is significantly faster and it allows frame rates higher than 100 Hz.

In terms of parameters, the image intensifier settings are controlled through the gain, which determines the MCP voltage and thus the signal magnification, and the gate opening. An external timer box was used to synchronise the image intensifier and the camera, thanks to which all the acquisition parameters of both instruments were controlled. The image were acquired at 500 Hz and the intensifier gate was varied between 0.4 and 0.7 ms, while the gain was kept constant at 700.

Chemiluminescence is a technique that doesn't require any calibration of the system. However, as it was previously done for the PIV measurements, a spatial calibration was performed to be able to accurately place the reaction zone inside the combustion chamber and monitor its movement (Fig. 3.6).

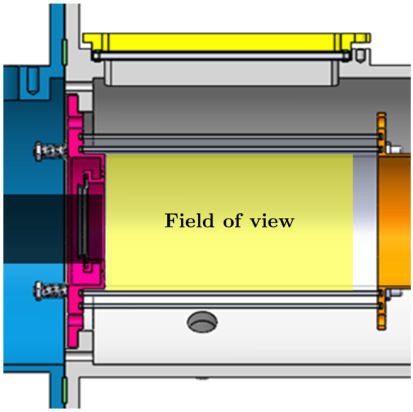

Figure 3.6: Chemiluminescence field of view

As it can be seen from Figure 3.3, the OH* emission band is superimposed to the broadband $CO^*{}_2$ emission. Thus, the application of the mentioned narrow bandpass filter on the camera lens doesn't avoid the acquisition of the broadband signal together with the wanted OH radical intensity. However, this won't affect the purpose of qualitatively identifying the reaction zone and analysing its variations with the operating conditions as the OH* contribution is far heavier than the broadband contribution of the $CO^*{}_2$. In addition, care must be taken during the analysis of the data as chemiluminescence is a line-of-sight technique. This means that the emission intensity collected by the camera is given by the contribution of all the chemiluminescence signals integrated along the ideal line that connects the camera sensor to the desired field of view. Normally, the intensity of the flame mid plane can be reconstructed in time averaged measurements through the application of an inverse Abel transformation, that takes advantage of the flame cylindrical symmetry to generate a deconvolution of the image intensity [44].

The acquired raw images were then post processed in MATLAB environment, as it will be further explained in the chemiluminescence result section.

Chapter 4

Flow Field Measurements

Contents

The burner flow field was firstly investigated in non reactive conditions. PIV measurements in reactive environments are quite more challenging compared to non reactive flows as additional optical noise coming from the flame luminosity further complicates an already laborious experiment.

One of the most challenging aspects is the handling of the seeding particles. In order to ensure a constant and uniform seeding density and avoid the formation of any particle clumps, several attempts were made in terms of valves configurations and seeder pressure to improve the quality of the experimental measurements. Furthermore, a major technical issue is related to the particle deposition along the optical liner surface generating an intense optical noise. This phenomenon was more severe in reactive conditions, possibly enhanced by high temperatures and water vapour formation during the reaction process. This issue was mitigated minimising the seeding quantity and its injection duration.

Therefore, the PIV system was optimised in terms of laser power, seeding quantity and camera settings in order to minimise unwanted optical noise. In addition to the set-up illustrated in section 3.1, a

polarising filter is placed in front of the bandpass filter of the camera lens to better manage the reflections caused by the cylindrical liner shape above all. The remaining background noise was eliminated through a dedicated background noise removal algorithm and the data were then post processed applying adaptive correlations and peak validations, as previously detailed in the measurement dedicated section.

4.1 Mean flow field

A first test campaign was performed at ambient conditions to assess the burner flow field at its symmetry plane (XY plane). The test campaign was replicated in reactive conditions at an adiabatic flame temperature of about 0.75 to compare the two resulting flow fields. The tested operating conditions are summarised in Table 4.1.

Table 4.1: PIV non reactive and reactive operating conditions

Parameter	Value
T_i	300 °C
ΔP	4.5%
T_{flame}	0.75
Fuel Split	100% RF

Figure 4.1a shows the mean velocity contours of the non reactive (left) and reactive (right) flow field, normalised with the maximum velocity value of the reactive case. The solid lines highlight the typical combustion chamber flow field for a swirl stabilised flame.

In both conditions, the swirling motion generated by the swirlers forces the flow to spread radially towards the chamber liner wall, creating a low velocity outer recirculation zone (ORZ) in the corner between the dome and the liner. The sudden expansion of the flow causes an increase in the vortex size and consequently a pressure rise in the vortex core, generating a positive pressure gradient in the central region of the combustion chamber. The flow field is therefore subject to a vortex breakdown (VB), characterised by a negative axial velocity in the central

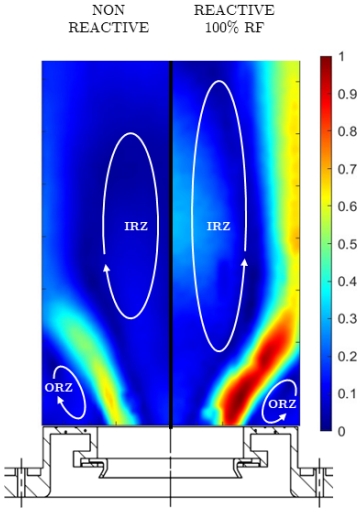

Figure 4.1: Normalised mean velocity contour with a schematic of the typical flow field (a) and with flow vectors (b) in non reactive conditions (left) and reactive conditions (right)

region of the combustion chamber [31, 45]. As a result, the flow develops an inner recirculation zone (IRZ) at the central part of the chamber. This region is fundamental for the flame stabilisation, as it continuously supplies heat and activated radicals from the hot combustion products towards the fresh mixture. In the area bounded by the outer and inner recirculation zone, the flow is accelerated and forms a shear layer (SL) between the high and low velocity regions generating high turbulence to enhance the mixing.

The flow field of both non reactive and reactive conditions in terms of vectors and mean velocity contours is reported in Figure 4.1b. As previously explained, the high velocity jet coming from the burner is pushed outwards and hits the liner wall. Therefore, a large inner recirculation zone is created highlighted by the dotted white line of the picture, corresponding to zero axial velocity. The IRZ origin and its initial interaction with the jets is not visible as it is anchored in the burner final dump region, close to the burner exit section as explained in Section 2.3. Similarly, it was not possible to collect information on the IRZ final part as it is located outside of the camera FoV, especially in reactive condition where the extension of the inner recirculation zone gets slightly larger.

Clearly, there is no big difference between non reactive and reactive conditions in terms of flow field features. The combustion process, thus the increase in temperature, leads to higher velocities. Furthermore, the thermal expansion and the lower densities of the reactive conditions cause an increase in the extension of the IRZ, especially in the radial direction. Also, in the reactive case, the flow entrapped in the inner recirculation zone moves back towards the burner with higher velocity compared to the non reactive case. This aspect together with the resulting larger extension of the IRZ forces the incoming high velocity jet outwards with a steeper angle. Consequently, the ORZ shortens and it is pushed closer to the burner wall.

4.2 Unsteady behaviour

Swirling flows are well known for their highly turbulent flow field that enhances the mixing process. Therefore, the burner flow field at its symmetry plane was also analysed from an unsteady point of view in statistical terms. The fluctuating velocity component (v') was extracted from the PIV measurements through Reynolds decomposition:

$$v = \bar{v} + v' \tag{4.1}$$

where v and $\bar{v}$ are respectively the instantaneous and the time-averaged velocity. The fluctuating part was then used to calculate the Root Mean Square (RMS) and the Turbulent Kinetic Energy (TKE), which is an essential factor in the flame stabilisation process:

$$RMS = \sqrt{\frac{1}{N}\sum_{n=1}^{N}[(v'_x)^2 + (v'_y)^2]} \tag{4.2}$$

$$TKE = \frac{1}{2}\left(\overline{v'_x{}^2} + \overline{v'_y{}^2}\right) \tag{4.3}$$

where N is the number of samples and v' and $\overline{v'}$ are respectively the fluctuating component and the average value of velocity along the spatial coordinates.

Figure 4.2a shows the RMS contour while Figure 4.2b displays the TKE on the burner symmetry plane for both the non reactive (left) and reactive (right) cases.

Immediately downstream the swirler, the turbulent kinetic energy reaches its maximum intensity creating two strips corresponding to the inner shear layer (ISL) and the outer shear layer (OSL), that respectively arise from the interaction with the IRZ and ORZ. The less turbulent region in between the two shear layers corresponds to the swirling jet core, through which the fresh mixture enters the combustion chamber. Further downstream, the interaction between the jet and the liner together with the blending of the two SLs generate a high TKE and high RMS spot and,

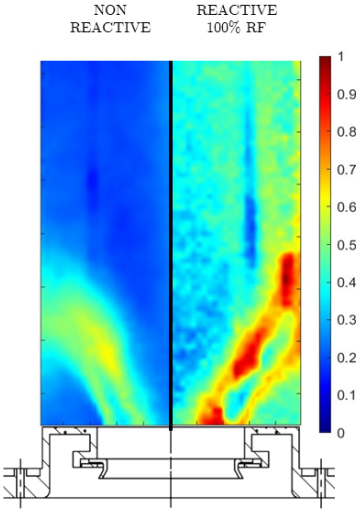

Figure 4.2: Normalised Root Mean Square of the velocity field (a) and Turbulent Kinetic Energy (b) in non reactive conditions (left) and reactive conditions (right)

consequently, a sort of wake along the liner surface characterised by a smooth decay of turbulent kinetic energy. Inside the IRZ, the turbulence level decrease noticeably, as it is necessary to ensure a stable combustion process.

Accordingly to the mean velocity contours, the RMS and TKE maps of the non reactive and reactive flow conditions are quite similar. The lower jet velocity of the non reactive case leads to shorter shear layers. In contrast to what happens in the reactive case, in non reactive conditions the shear layers merge before impacting the liner, reducing the extension of the jet core.

Chapter 5

Burner Characterisation

Contents

The burner flame structure and position were investigated through OH* chemiluminescence measurements. In addition, NO_x emissions were recoded at the same time to characterise the burner performance in terms of pollutant emissions. For a complete characterisation, the burner was also studied from a stability point of view through lean blow out (LBO) measurements.

In the next section, the tested operating conditions will be summarised and numbered for an easier and more straightforward reference and comparison between the various cases. Then, the flame shape and its variation with the tested operating conditions will be analysed, together with the relative pollutant emissions. Finally, the burner stability limits will be presented.

5.1 Tested operating conditions

The flame behaviour was recorded at different operating conditions in terms of flame temperature and burner fuel flow split, as it is summarised in Table 5.1. All the tests have been conducted at the same air inlet temperature of about 300 °C and the pressure drop along the combustor was fixed at 4.5%. In the first three tests, the burner was tested at three increasing flame temperatures and the fuel flow split was kept constant, feeding only the radial fuel line. On the contrary, analysing Cases 3 to 6, the flame shape variations were studied at the same flame temperature but with different flow split configurations. The axial fuel line was not further fed to not exceed Case 6 fuel split configuration as it was selected as the most favourable one in terms of NO_x emissions during the burner development process [33–35].

Table 5.1: Burner operating conditions for the OH chemiluminescence measurements*

Case	T_{flame}	Fuel split
1	0.75	100% RF
2	0.86	100% RF
3	1	100% RF
4	1	60% RF - 40% AF
5	1	50% RF - 50% AF
6	1	40% RF - 60% AF

5.2 OH* chemiluminescence results

OH* chemiluminescence images were acquired at 500 Hz recording about 900 images. The instantaneous snapshots were averaged to remove the influence of any unsteady phenomena and analyse the flame steady state structure. In addition, the averaging process smooths out the chemiluminescence intensity peaks associated with unsteady structures and reduce the measurement noise.

As previously explained in Section 3.2.1, chemiluminescence imaging is used to qualitatively study and locate the flame reaction zone. Thus, the absolute values of chemiluminescence intensity have no physical meaning and they are strongly dependent on the type of camera and intensifier employed for the testing and their relative settings. Throughout this test campaign, the intensifier gain was kept constant at 700 while the gate was varied between 0.4 and 0.7 ms depending on the flame luminosity (i.e. tested conditions). The latter directly affects the acquired pixel intensity. Due to the lack of information about the intensifier linear response characteristics, only the images recorded with the same intensifier settings were directly compared. For the cases acquired with different intensifier gate values, each averaged test condition was normalised over its maximum intensity value. Thanks to this operation, the aforementioned cases were compared in terms of flame shape and position and extension of the reaction zone.

In Figure 5.1, OH* chemiluminescence contour of Case 1 (Fig. 5.1a), Case 2 (Fig. 5.1b) and Case 3 (Fig. 5.1c) are compared. The main reaction zone can be identified through the high OH* chemiluminescence values. The flame temperature is raised by increasing the amount of fuel that flows through the radial fuel line, leading to a richer mixture. This modifies the fuel jet penetration and consequently the flame stabilisation region. As the jet penetration increases, the flame stabilises further downstream the burner exit section assuming the lifted shape visible in Figure 5.1c. As a result, the peak of chemiluminescence intensity moves accordingly and it gets closer to the liner walls. From Case 1 to Case 3, the shape of the reaction zone first gets slightly larger and bigger and then changes shape, becoming more squeezed and moving away from the burner tip.

Chemiluminescence trends were also analysed along the liner at six different locations equally spaced from the burner exit, as indicated in Figure 5.2. Figure 5.3 shows the chemiluminescence intensity profiles along the normalised burner radius for Case 1 to 3. The locations of the chemiluminescence intensity peaks were analysed to gather informations on the reaction process.

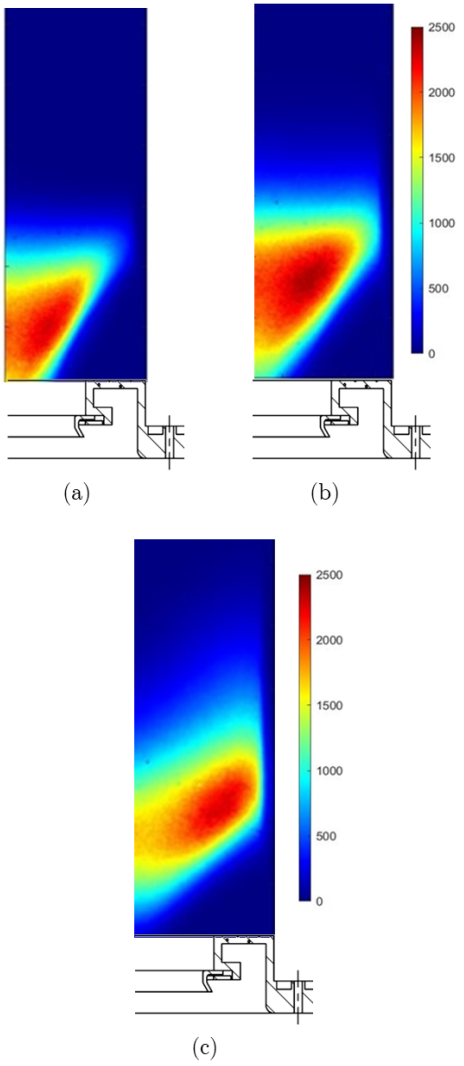

Figure 5.1: OH chemiluminescence contour at 100% RF at three different flame temperatures: (a) at $T_{flame} = 0.75$, (b) at $T_{flame} = 0.86$, (c) at $T_{flame} = 1$*

As the flame temperature increases, the peak is located further downstream: Case 1 intensity peak is closer to the burner exit near plane 2, Case 2 maximum chemiluminescence value is found around plane 3 while the peak of Case 3 was detected along location 5. Case 1 ad 2 have pretty similar trends, while the increased jet penetration of Case 3 shifts the flame position. Indeed, because of its lifted shape, the chemiluminescence intensity of Case 3 around section 1 and 2 is much lower than the other two analysed cases, while it gets much higher further away.

As pointed out from the OH* images, the peak locations vary not only along the length of the liner but also along the burner radius. In Case 1 and 2 the highest chemiluminescence intensity is closer to the burner central axis, at a radius of about 0.3. On the contrary, the reaction zone of Case 3 is larger and the intensity peaks moves to bigger radius, of about 0.5.

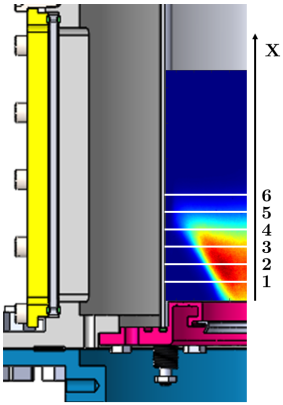

Figure 5.2: Measurements planes used for the chemiluminescence trends analysis

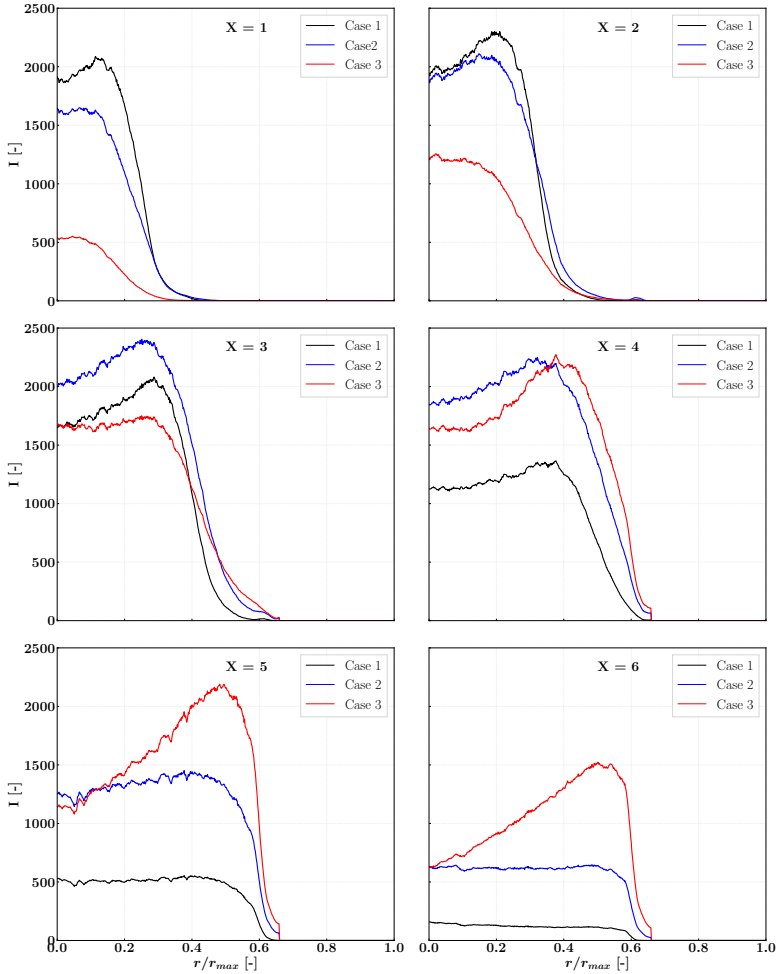

Figure 5.3: OH chemiluminescence intensity trends along the burner normalised radius at 6 equally spaced locations downstream the burner exit section for Case 1 to 3*

To gain a better understanding on the flame anchoring position, the PIV measurements presented in the previous chapter were analysed together with the OH* contour of Case 1 as the experiment were conducted at the same operating conditions. However, since chemiluminescence is a line-of-sight technique, the chemiluminescence measurements need to be properly post processed to be directly compared to the flow field. Ignoring the flame self absorption contribution and assuming an axisymmetric flame, the time averaged OH* chemiluminescence measurement were used to recreate the intensity distribution on the burner symmetry plane with deconvolution algorithms such as the inverse Abel transform. More details about the algorithm can be found in [44].

OH* chemiluminescence intensity isolines at the highest chemiluminescence intensities were then isolated to define the flame position. Figure 5.4a shows the Abel transformed chemiluminescence intensity isolines with the vectors of the velocity field retrieved from the PIV measurements on the burner symmetry plane. The flame clearly anchors in the inner shear layer region where high turbulence is promoted through the interaction between the IRZ and the jet flow exiting the burner, as also highlighted by the turbulent kinetic energy distribution of Figure 5.4b.

The effect of the burner fuel split between the axial and the radial line on the flame structure was then investigated. As mentioned previously, the adiabatic flame temperature was kept constant at 1 and the two fuel lines were fed in various combination. Increasing the axial line content, the flame luminosity noticeably diminished. The gate intensifier was augmented accordingly to be able to measure properly the OH* chemiluminescence intensity. The averaged data were then normalised as explained at the beginning of this section to compare the results.

In Figure 5.5, OH* chemiluminescence maps of Case 3 (Fig. 5.5a), Case 4 (Fig. 5.5b), Case 5 (Fig. 5.5c) and Case 6 (Fig. 5.5d) are shown: moving from figure a to d the fuel content on the radial line is decreased from 100% to 40% and the axial fuel line is increased consequently. As the amount of fuel flowing through the radial line diminishes, the flame anchors back in the central region closer to the burner exit. This behaviour

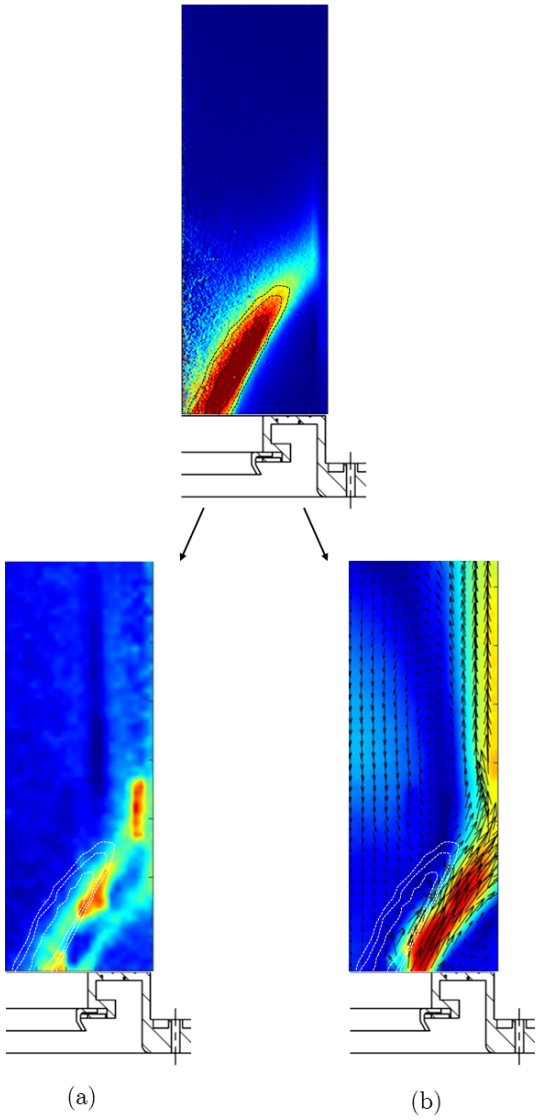

Figure 5.4: Abel transformed OH chemiluminescence intensity isolines of Case 1, superposed by the Turbulent Kinetic Energy map (a) and velocity contour with flow vectors of the PIV measurements (b)*

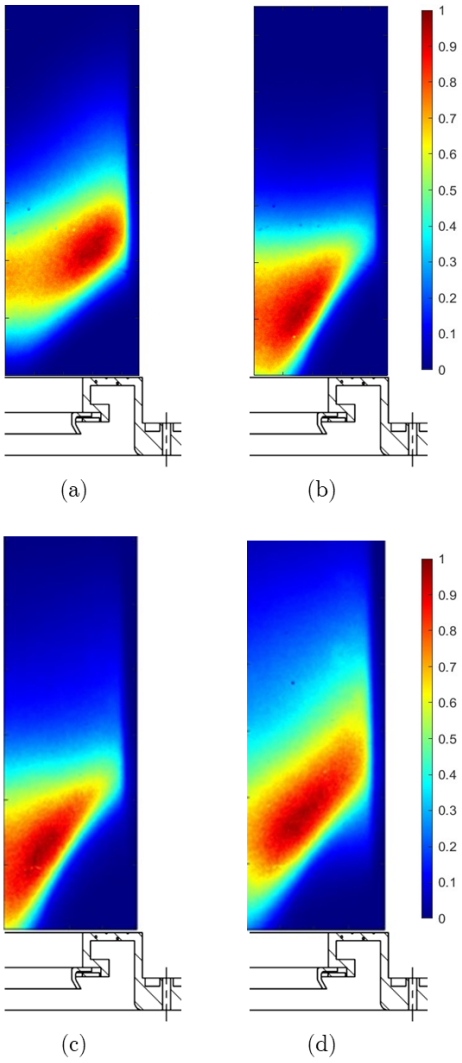

Figure 5.5: Normalised OH chemiluminescence contour at $T_{flame} = 1$ at four different fuel splits conditions: (a) 100% RF, (b) 60% RF - 40% AF, (c) 50% RF - 50% AF, (d) 40% RF - 60% AF*

endures until the last tested fuel flow split, where the amount of fuel through the axial fuel line is grater than the radial one.

The experienced variation in flame shape is mainly driven by the fuel jet velocity of the radial line. When the total fuel amount flows through the radial line, the fuel velocity is higher than the fresh air thus the flame stabilisation happens downstream the burner exit section, assuming a lifted shape. In Figure 5.5b and 5.5c, the fuel stream through the radial line decreases and its exiting velocity is low enough for the fuel to get entrapped in the recirculation zone created in the dump region of the burner (Fig. 2.8). Indeed, the channel throat after the radial line location provide the mixture with the proper acceleration through the downstream sudden section expansion, where the flame then anchors. However, in the last case the radial line equivalence ratio gets leaner and the flame behaviour starts shifting back towards a lifted configuration. Thus, in Figure 5.5d the reaction zone lengthens, relocating the flame a little downstream. Also, the chemiluminescence intensity peak moves away from the liner wall as the radial line fuel starts decreasing and start shifting again towards the liner only in the last case. Actually, the flame shape of Figure 5.5a and 5.5d are quite similar: the reaction zone gets shorter as it spreads more radially, interacting more with the combustion chamber walls.

As it was previously done for the flame temperature comparison, the OH* chemiluminescence trends were analysed at the same six locations along the liner (Fig. 5.2). The normalised OH* chemiluminescence intensity is plotted along the normalised burner radius in Figure 5.6 for Case 3 to Case 6. Case 4 and Case 5 normalised intensity almost follows the same trends at all locations, confirming the close behaviour of the aforementioned fuel splits. The chemiluminescence peak is in both cases located around plane 2 and close to the burner central axis ($r/r_{max} = 0.2$), as it was found for Case 1 and 2, proving a comparable flame behaviour.

Similarly, the chemiluminescence plots of Case 3 and Case 6 follow the same trend. The flame observed in Case 3 is more lifted, indeed the chemiluminescence values are the lowest ones registered close to the

burner mouth. Starting from plane 4 the trends are almost superimposed and both peaks are found at a burner radius of 0.4 around plane 4, proving the wider extension of the reaction zone already pointed out during the OH* maps analysis.

5.3 Emissions

During the chemiluminescence assessment, pollutant emissions were measured as illustrated in Section 2.1. Therefore all the previous cases were analysed to assess the impact of both the flame temperature and the fuel split on emissions.

Figure 5.7 and 5.8 show respectively the CO and NO_x emissions as a function of the normalised flame temperature at constant split (Case 1 to 3). As expected, CO emissions decrease at higher flame temperature. Actually, analysing the chemiluminescence maps of Figure 5.1 it is clearly visible that at leaner conditions the flame gets closer to the burner exit section, creating an initial richer zone. In this area, the poor fuel-air mixing is responsible for the evident increase in CO emissions. At higher flame temperature, even though the flame interacts with the liner wall that cools down the mixture blocking the reaction progress, the flame anchors in a different position and the better mixing contributes to the CO emissions abatement.

The trend of NO_x emissions remains almost flat, assuming almost a constant value around 11 ppm for the lowest and highest flame temperature while a slight increase in NO_x emissions is visible for the medium case. Analysing once again the chemiluminescence measurements (Fig. 5.1), Case 2 shows a higher chemiluminescence intensity compared to the other two tested flame temperatures which corresponds to a higher reactivity, responsible for the small increase in NO_x emissions.

The emissions trends were also analysed at various fuel split conditions at constant adiabatic flame temperature (Case 3 to 6). Figure 5.9 and Figure 5.10 illustrate the CO and NO_x emissions as a function of the radial fuel line split.

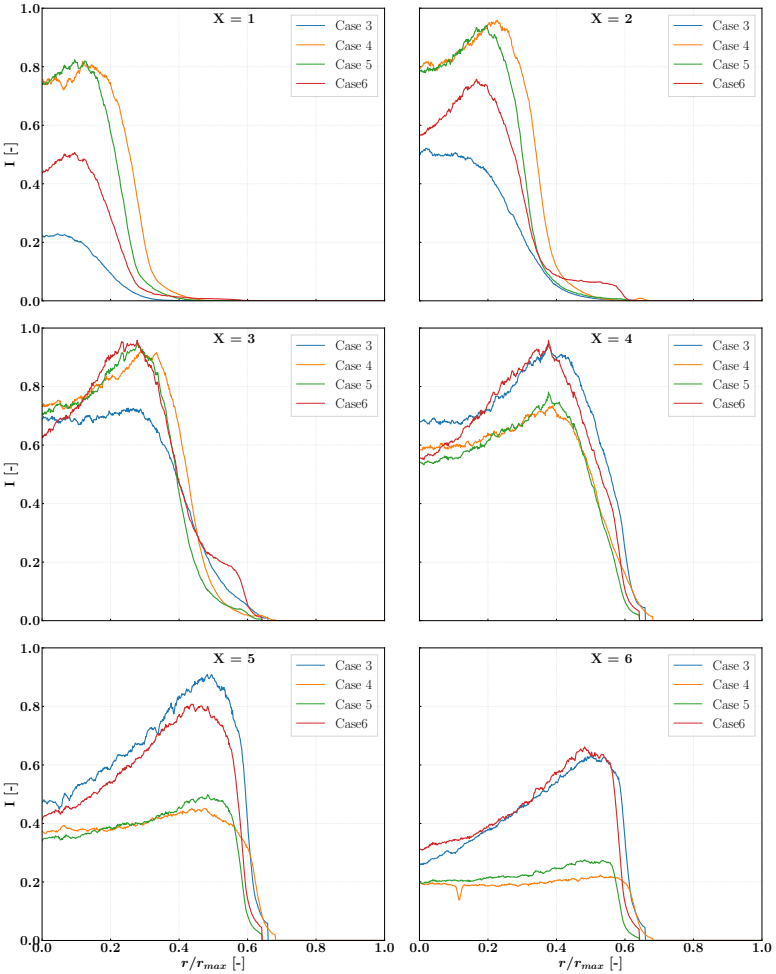

Figure 5.6: OH chemiluminescence intensity trends along the burner normalised radius at 6 equally spaced locations downstream the burner exit section for Case 3 to 6*

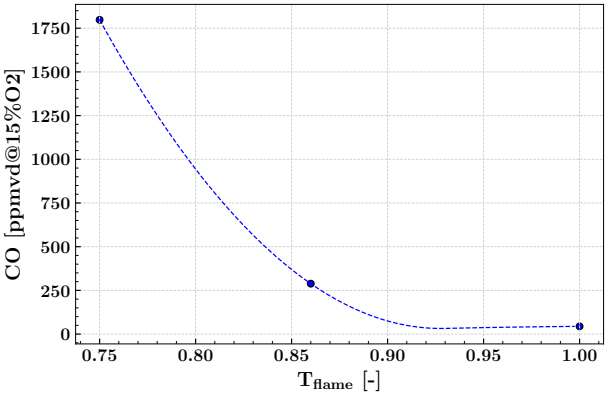

Figure 5.7: CO emissions as a function of the adiabatic flame temperature

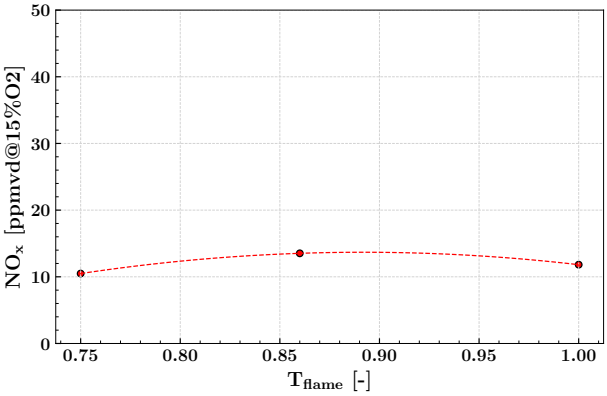

Figure 5.8: NO_x emissions as a function of the adiabatic flame temperature

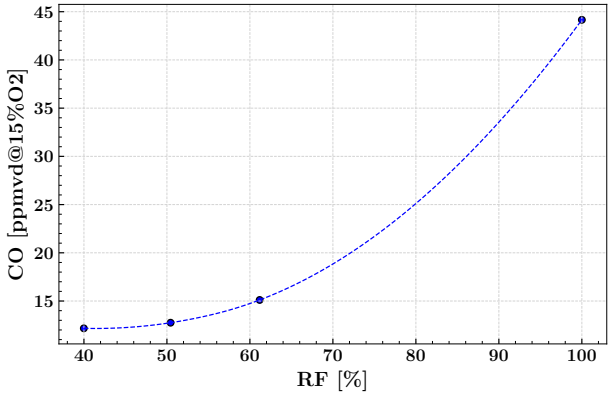

Figure 5.9: CO emissions as a function the amount of fuel flowing through the radial fuel line (RF)

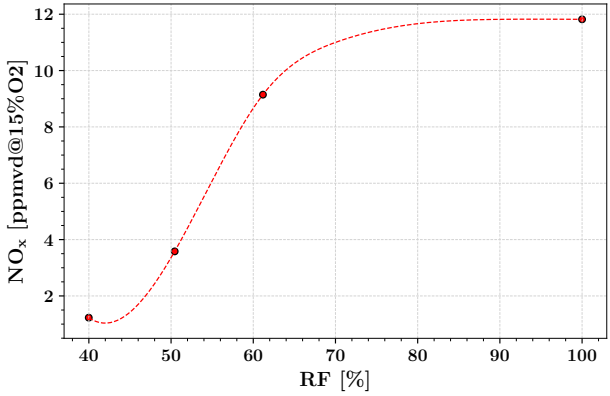

Figure 5.10: NO_x emissions as a function the amount of fuel flowing through the radial fuel line (RF)

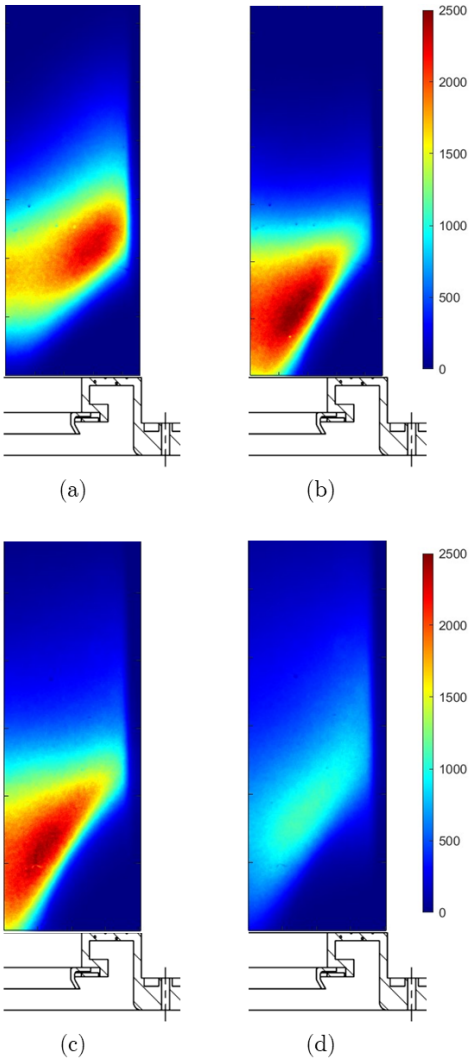

Figure 5.11: OH chemiluminescence contour at $T_{flame} = 1$ at four different fuel splits conditions: (a) 100% RF, (b) 60% RF - 40% AF, (c) 50% RF - 50% AF, (d) 40% RF - 60% AF*

In Figure 5.9, a peak in CO emissions can be found at 100% RF. As it was explained for the trend obtained at different adiabatic flame temperatures, looking at the chemiluminescence of Figure 5.5 it is possible to see the change in shape that the flame experience from 100% to 40% RF. Moving from Case 3 to Case 4, there is an initial marked drop in CO emissions due to an enhanced mixing promoted by the axial stream. A further increase in the axial fuel line content, still benefit CO emissions but at a lesser extent and the trend assumes an asymptotic behaviour.

Similarly, NO_x emissions decrease as the AF contribution grows. The favourable effect of the better mixing linked to the activation of the premix line can be appreciated already from small amount of AF content, leading to a reduction in NO_x emissions by a factor of 4 from 100% RF to 60% RF. The trend then stabilises and reaches a minimum of about 1 ppm at 40% RF. Therefore, a fuel split biased towards the axial fuel line reduces the radial line equivalence ratio, which is responsible for the majority of the NO_x emissions formation. Indeed, Figure 5.5 shows the normalised chemiluminescence but looking at the chemiluminescence maps of Figure 5.11 it is clearly visible that the fame reactivity lessens as the radial line content is decreased. However, as the radial line is mainly responsible for the flame anchoring and stabilisation, a balance must be found to ensure a stable combustion at the same time.

5.4 Stability limits

One of the most important aspects in a burner design is its capacity to provide stable combustion. Wider stability limits allow the combustor to operate in leaner conditions, reducing thus the adiabatic flame temperature and consequently NO_x emissions.

The flame stability was investigated during this test campaign to assess the burner behaviour. Lean blow tests were carried out to determine the burner stability limits in different radial-axial split configuration, namely Case 3 to 6. For each case, starting from stable conditions, the air mass flow rate was gradually increased while maintaining the pressure drop

across the combustion chamber within an acceptable range, until the flame extinguishes. The blow out event was detected observing the flame and then the flow conditions at the blow out were derived post processing the thermocouples readings. Indeed, the thermocouples installed right after the quartz liner are a good indicator of the blow out event as they quickly sense a sudden drop in temperature when the flame extinguishes. The instant right before the abrupt change in the temperature trend was selected as the lean blow and the corresponding flow conditions were retrieved.

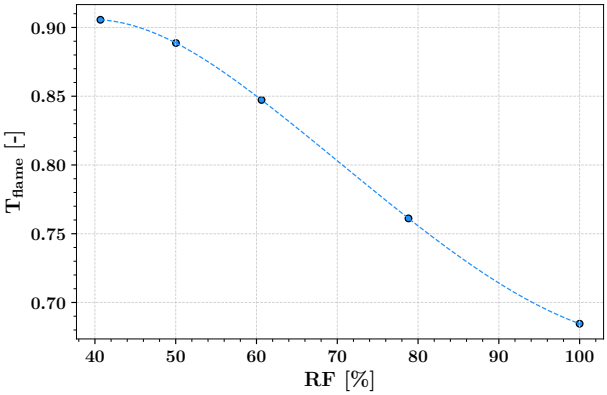

Figure 5.12: Lean Blow Out measurements expressed as corresponding adiabatic flame temperature as a function the amount of fuel flowing through the radial fuel line (RF)

Figure 5.12 shows the burner stability limits in terms of adiabatic flame temperature (T_{flame}) as a function of the fuel split, identified as the amount of fuel flowing through the radial fuel line (RF %). Looking at the two limiting conditions, for the 100% RF case the flame remained stable until the adiabatic flame temperature reached a value below 0.65. Differently, only a T_{flame} of 0.85 was reached for the 40 % RF case. Indeed, as the axial line content increases, the blow out margin decreases and the burner moves to a more unstable condition.

This behaviour is aligned with the chemiluminescence measurements analysed in the previous section. As derived from the chemiluminescence measurements, the radial line is responsible for the flame stabilisation so when its contribution diminishes the flame is less stable and the blow out margin decreases accordingly. Indeed, going from Case 3 to Case 6, the OH* luminosity experiences a considerable reduction indicating a lower flame reactivity that negatively affects the flame stability. In the previous section, Case 6 which corresponds to the highest AF content is the most promising in terms of NO_x emissions but on the contrary it is the worst configuration in terms of stability limits. The axial line globally provides a better mixing achieving a more uniform fuel distribution, which is an important aspect in terms of emissions but at the same time it is detrimental for the flame stability as richer regions are responsible for the flame stabilisation.

Therefore, to achieve a wider low NO_x emissions regulating window, a wider blow out margin that allow for a reduction in adiabatic flame temperature is indeed an essential characteristic of the burner aerothermal design.

Chemiluminescence images were also acquired throughout the test with a sample frequency of 500 Hz in order to gather some information of any pulsation the flame could experience or precursor behaviour that might indicate the approaching of the lean blow out. As an example, a sequence of snapshots of 100% RF case are plotted in Figure 5.13. As expected, the flame experience some random oscillations. However, prior the LBO, no extinction and reignition process is observed: the flame loss is quick and sudden and no LBO precursor were discovered at any of the cases investigated.

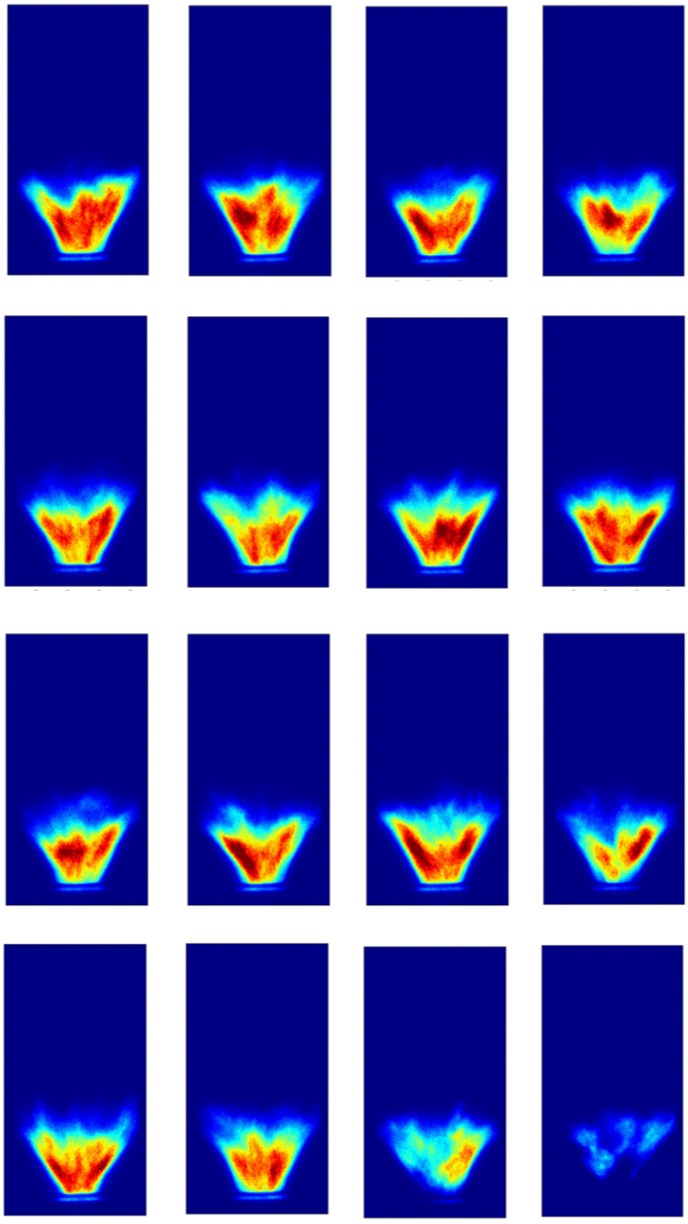

Figure 5.13: Sequence of OH chemiluminescence images at 100% RF at increasing oxidiser mass flow content until the lean blow out is reached (acquisition frequency 500 Hz)*

Chapter 6

Combustion in vitiated air conditions

Contents

In this section the experiment performed with CO_2 addition will be presented. As explained in Chapter 1, CO_2 was added into the main airflow to simulate EGR conditions. The CO_2 merges with the main incoming airflow prior the electric heater (Fig. 2.1) in order to ensure an homogeneous mixture, both in terms of concentrations and temperature. This experimental campaign aims at testing the burner adaptability at different operating conditions and understand the potential modification needed to operate in such an oxygen depleted environment.

The CO_2 content was gradually increased to decrease the oxygen content available for the combustion process. Four different operating conditions in terms of available oxygen concentration in the incoming airflow were tested. In order to derive a truthful comparison on the burner behaviour, the adiabatic flame temperature was kept constant at

all conditions adjusting the fuel flow. Particular attention was drawn towards the chamber pressure drop, that was closely monitored during the experiments as the CO_2 addition may cause a little variation on the defined operating pressure drop. However, the experienced variations were considered small enough to not cause any undesirable alteration on the flame behaviour.

First of all, the burner was studied from a stability point of view through lean blow out (LBO) measurements. As it will be further detailed in the dedicated section, the air was vitiated to define the burner stability limits finding the maximum tolerated amount of CO_2 for stable combustion. Then, the flame position and structure were analysed mainly through OH* chemiluminescence measurements. As it was done previously for the burner characterisation, emissions were measured as well to evaluate the burner performance in terms of pollutant emissions. All the tested conditions will be presented and summarised in a specific section for a clearer comparison. In addition, all measurements in vitiated air conditions will be compared to the previous measurements conducted in regular operating conditions.

6.1 Burner stability limits

One of the principal issues related to the EGR feasibility is the flame stability. Indeed, the addition of CO_2 into the incoming airflow reduces the amount of available oxygen for the combustion process, weakening the flame stability.
Therefore, initially the flame blow out margin was studied in order to derive the maximum allowable CO_2 concentration to ensure stable combustion in different fuel flow split configurations. Similarly to the procedure adopted for the burner characterisation, for each tested condition the fuel flow was kept constant and the CO_2 content was increased until the flame extinguished. Little variations in terms of combustion chamber pressure drop were experienced, but attention was paid to keep them in a reasonable range to not affect the burner behaviour.

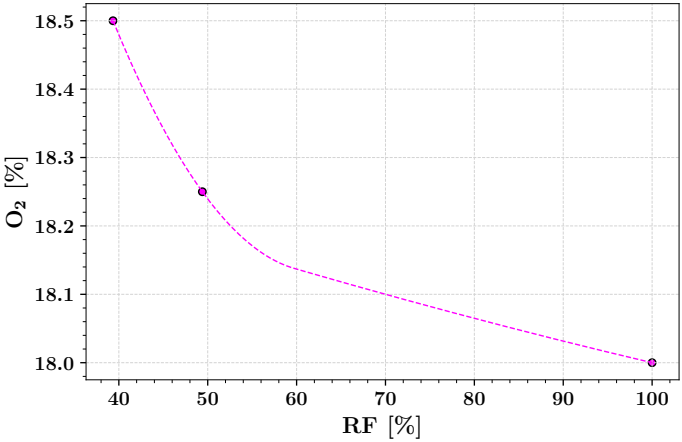

Figure 6.1: Lean Blow Out measurements expressed in terms of oxidant oxygen content as a function of the amount of fuel flowing through the radial fuel line (RF)

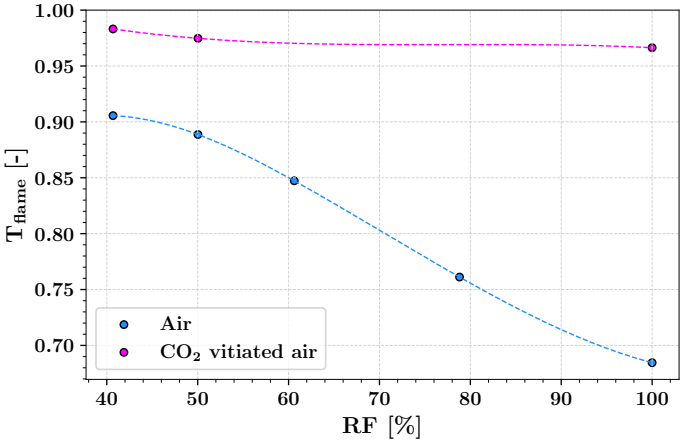

Figure 6.2: Lean Blow Out measurements expressed in terms normalised flame temperature for standard air and vitiated air conditions as a function of fuel flow content of the radial fuel line (RF)

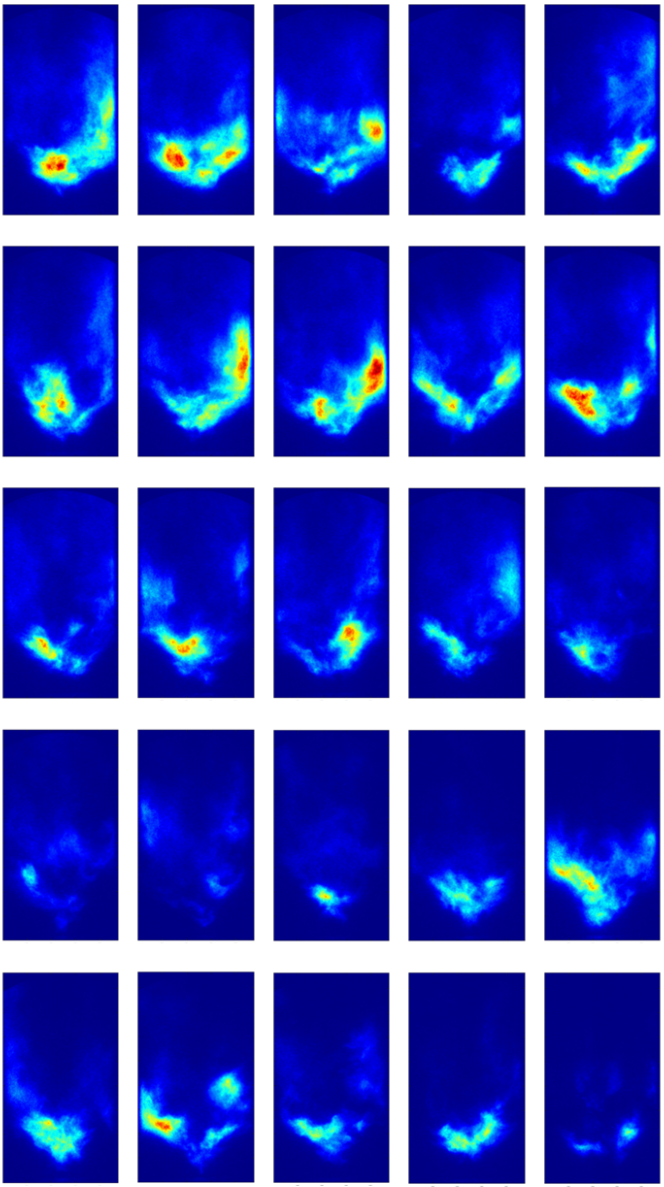

Figure 6.3: Sequence of OH chemiluminescence images at 100% RF at increasing CO_2 oxidant content until the lean blow out is reached (acquisition frequency 500 Hz)*

Figure 6.1 shows the burner blow out margins in terms of oxidant oxygen content as a function of the fuel flow split, expressed in terms of radial line content. As the radial fuel flow diminishes, the minimum oxidant oxygen content increases to ensure flame stability. Indeed, as shown in the burner characterisation both from chemiluminescence measurements and stability limits, the radial fuel helps the flame anchoring and stabilisation process. Thus, at 100% RF the minimum oxygen molar concentration in the oxidant mixture reaches the lowest experienced value at about 18%. The oxygen molar concentration necessary for a stable combustion increases as the axial fuel stream grows, reaching a value of about 18.45% for the 40% RF - 60% AF fuel split case.

The so found blow out margins were then compared to the stability limits identified in standard air conditions. In order to do so, the results are expressed in terms of adiabatic flame temperature, normalised with the same reference condition used throughout the investigation. In Figure 6.2, the lean blow out margins of both oxidant conditions are compared at different fuel flow split. In vitiated air conditions, the curve seems almost flat and the minimum adiabatic flame temperature to ensure stable combustion reaches much greater values compared to the standard air case. Indeed, lowering the availability of oxygen for the combustion process worsen the flame stability at all fuel split conditions, indicating that the increase of the radial fuel line content does not improve remarkably the flame stability.

These information were used to define the most interesting configurations to be further analysed in terms of flame shape through OH* chemiluminescence measurements and pollutant emissions. As pointed out previously, the most unstable condition is the one at greatest axial line content and it drives the maximum CO_2 oxidant content tested. Therefore, to ensure stable combustion, a 18.5% oxygen molar concentration was chosen as lowest allowable oxygen oxidant content to be investigated during the burner characterisation in vitiated air conditions.

In addition, OH* chemiluminescence images were acquired throughout the test with a sample frequency of 500 Hz, as it was previously done for

standard air conditions. Similarly, the intent was to find any particular behaviour that indicates the approaching of the extinction limit or the LBO event beforehand. The 100% RF fuel flow split is taken as example and a series of OH* chemiluminescence images are showed in Figure 6.3. Once again, no evidence of LBO precursor behaviour is observed nor extinction and reignition process. Some random oscillations are detected and the flame loss happens all of a sudden at all the investigated fuel flow splits.

6.2 Tested operating conditions

The burner was tested under different EGR conditions, at decreasing oxygen concentration available for combustion while keeping the same adiabatic flame temperature ($T_{flame} = 1$). As the fuel split was found to play an important role both in the flame shape definition and in terms of pollutant emissions, the various CO_2 concentrations were also tested at different fuel flow split. Once again, the combustion chamber pressure drop was kept constant around 4.5% and the temperature of the incoming air and CO_2 mixture was fixed at 300 °C.

Table 6.1: EGR tested operating conditions for the OH chemiluminescence measurements*

Case	T_{flame}	Fuel split	Oxygen (mol)
7	1	100% RF	19.5%
8	1	100% RF	19%
9	1	100% RF	18.5%
10	1	50% RF - 50% AF	20%
11	1	50% RF - 50% AF	19.5%
12	1	50% RF - 50% AF	19%
13	1	50% RF - 50% AF	18.5%
14	1	40% RF - 60% AF	20%
15	1	40% RF - 60% AF	19.5%
16	1	40% RF - 60% AF	19%
17	1	40% RF - 60% AF	18.5%

All the conditions are summarised in Table 6.1. The lowest reachable oxygen content was selected after the burner stability limits investigations. As explained in the dedicated section, starting from the worst case scenario represented by the 40% RF - 60% AF fuel flow split, the minimum oxygen molar fraction was set to 18.5% in order to ensure steady state conditions for the flame shape investigations and emission measurements. In Cases 7 to 9, the burner fuel flow was injected only though the radial fuel line and the oxygen content was varied between 19.5% and 18.5%. A wider range of oxidiser mixtures was tested for the other two fuel split selected configurations, as they are more prone to instabilities.

6.3 OH* chemiluminescence measurements

The flame structure and position variations were qualitatively studied through OH* chemiluminescence measurements to locate the flame reaction zone. About 900 images were acquired at 500 Hz for each tested condition. The same settings and post process applied during the burner characterisation were employed here to analyse the recordings. Therefore, the instantaneous snapshots were averaged to remove the influence of any unsteady phenomena and analyse the flame steady state structure. Once again, it's worth pointing out that chemiluminescence intensity values do not represent any quantitative information about the radical of interest or the flame itself. The intensifier gain was kept constant at a value of 700 in this test campaign too. The intensifier settings were adjusted depending on the flame luminosity by choosing a proper gating. As explained in chapter 5.2, this parameter directly affects the resulting pixel intensity so only the images acquired with the same gating can be directly compared. The images recorded with different intensifier gate values were therefore normalised over their maximum intensity value to analyse the differences in the reaction zone shape and extension.

Figure 6.4 shows OH* chemiluminescence contour for Cases 10 to 13, where the fuel flow split was kept constant at 50%. From left to right, the oxygen content available for combustion was reduced and images

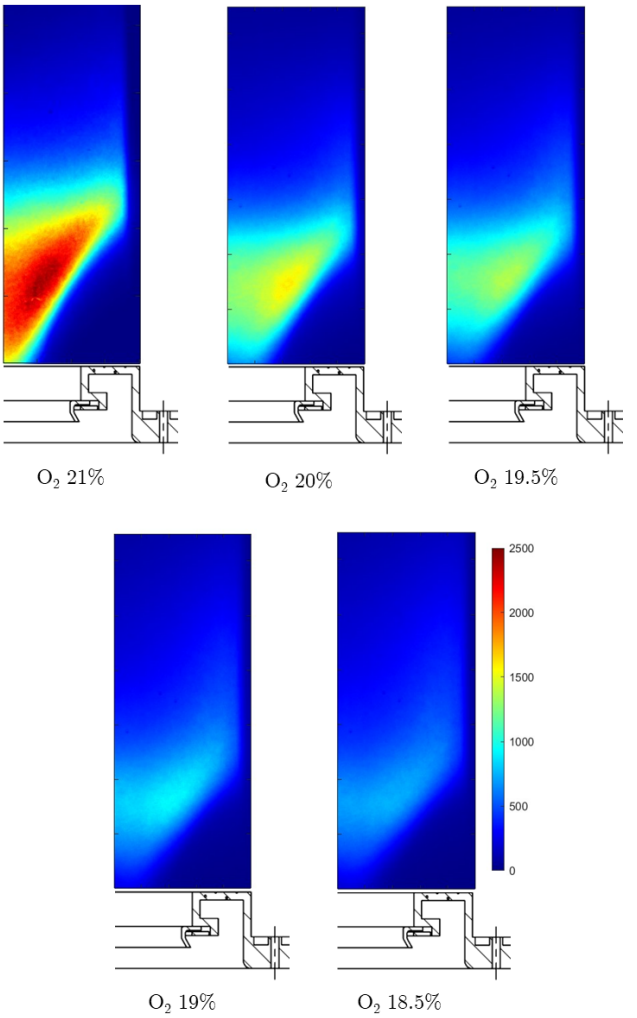

Figure 6.4: OH chemiluminescence contour at 50% RF - 50% AF at decreasing oxygen content*

were acquired once steady state conditions were reached. The intensifier gate was kept constant with the purpose of illustrating the enormous difference in terms of chemiluminescence intensity. Indeed, as the available oxygen diminishes the chemiluminescence intensity drops rapidly and the reaction zone is barely visible at 18.5% oxygen molar concentration. As expected, the limited amount of oxygen available for the combustion process reduces dramatically the mixture reactivity. The same behaviour was also experienced at the other fuel flow splits configurations.

For a better comparison, in Figure 6.5 the normalised chemiluminescence measurements between standard air condition and vitiated air at 19.5% oxygen molar concentration is presented for each tested fuel flow split. This time the maps were normalised with the above mentioned procedure to define more clearly the combustion reaction zone.
Analysing the 100% RF fuel flow split, it is clearly visible that the flame stabilises further downstream in the CO_2 addition case. This implies a lower reactivity that causes a delay in the chemical reaction process. For the same reason, in terms of shape, the flame seems a little longer with no additional major differences. The same conclusions can be drawn looking at the central image where the two conditions for the 50% RF - 50% AF case are reported. Small differences can be appreciated in terms of flame shape.

With regards to the last analysed split, which was selected as the most promising configuration in terms of emissions during the burner characterisation, the flame morphology experience a radical change. The combined effect of the axial fuel line increase and the oxygen content depletion leads to a delay of the reaction process. Indeed, the reaction zone becomes more widespread, reaching an extension that almost cover the whole quartz combustion chamber. This change in the reaction zone shape and location could be related to the Damköhler number (Da), which represents the flow to chemical time scale ratio. This dimensionless number is used to characterise to turbulence-chemistry interaction: a high Da number indicates mixing controlled flames while as the Da number decreases, the chemical reactions becomes slower. The CO_2 addition

doesn't alter the flow field in terms of turbulence, thus the flow time scale is not affected. Whilst, as observed in the OH radical distributions, the reaction time scale increases and it moves the reaction away from the burner exit, suppressing the process of the oxidation reaction.

The get a deeper insight on the effect of the air vitiation on the flame position, the OH* chemiluminescence intensities were plot along the liner at the same planes defined during the burner characterisation (Fig. 5.2). For each fuel split, both the trend of standard air and vitiated air conditions are plotted along the normalised burner radius. Starting from the 100% RF fuel split, in Figure 6.6 Cases 3 and Case 7 are compared. The delay in the chemical reaction progress is perfectly noticeable: the curve shape is quite similar but shifted in space. Indeed, the chemiluminescence peak intensity is reached around section 4 for Case 3 and section 5 for Case 7, at the same position in terms of burner radius.

The same behaviour can be found analysing Figure 6.7, where the trend of the 50% RF - 50% AF fuel split case are plotted. However, the peak of plane 3 for the oxygen depleted oxidiser case is less marked: the difference between the intensity value at the burner center line ($r/r_{max} = 0$) and the maximum one of Case 11 is smaller than the variations registered in standard air conditions.

Analysing the 40% RF - 60% AF fuel split case, Figure 6.8 confirms the flame change in shape for the CO_2 addition case. Indeed, the trend of Case 15 are smoother and a peak is not really defined. In addition, as clearly visible from the chemiluminescence maps, high chemiluminescence values can be found also around section 6, while a decrease in intensity was experienced in all the previous analysed cases moving from plane 5 to plane 6. This further confirms the change in combustion regime, as the reaction zone is more widespread both along the burner radius and along the liner

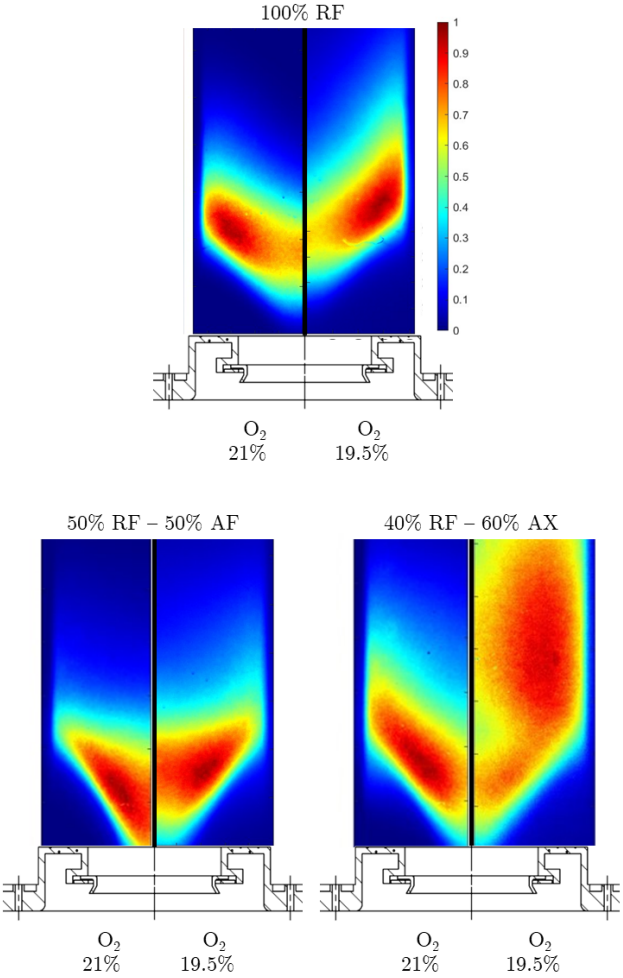

Figure 6.5: Comparison between OH chemiluminescence measurements at various fuel fuel split in normal (left) and vitiated air conditions (right)*

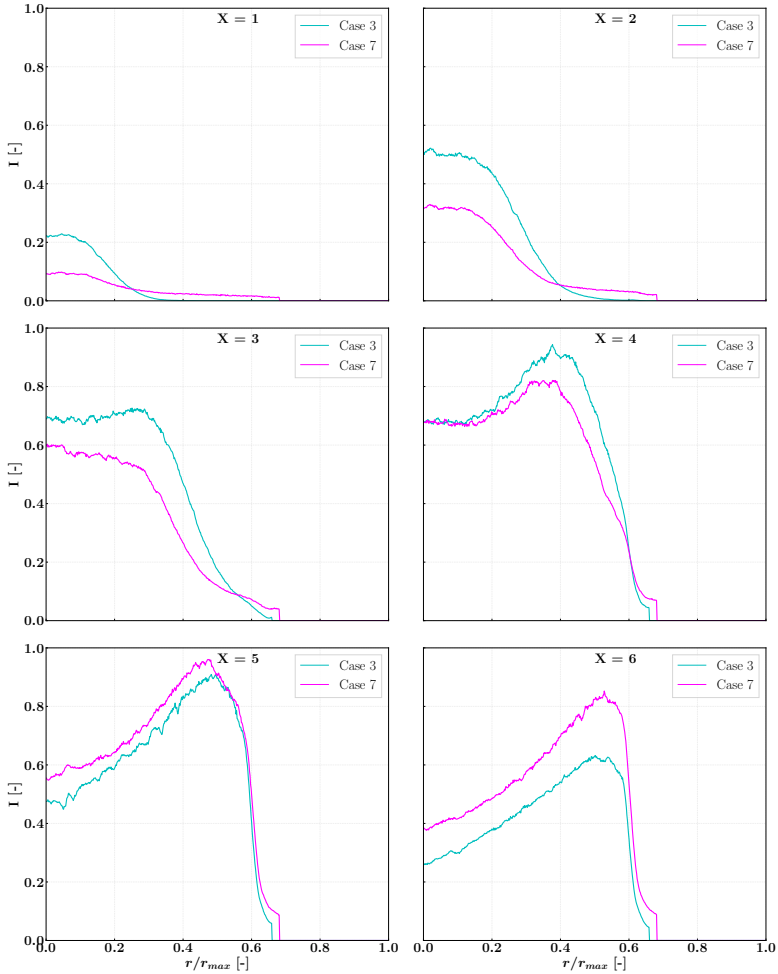

Figure 6.6: OH chemiluminescence intensity trends along the burner normalised radius at 6 equally spaced locations downstream the burner exit section for Case 3 and 7*

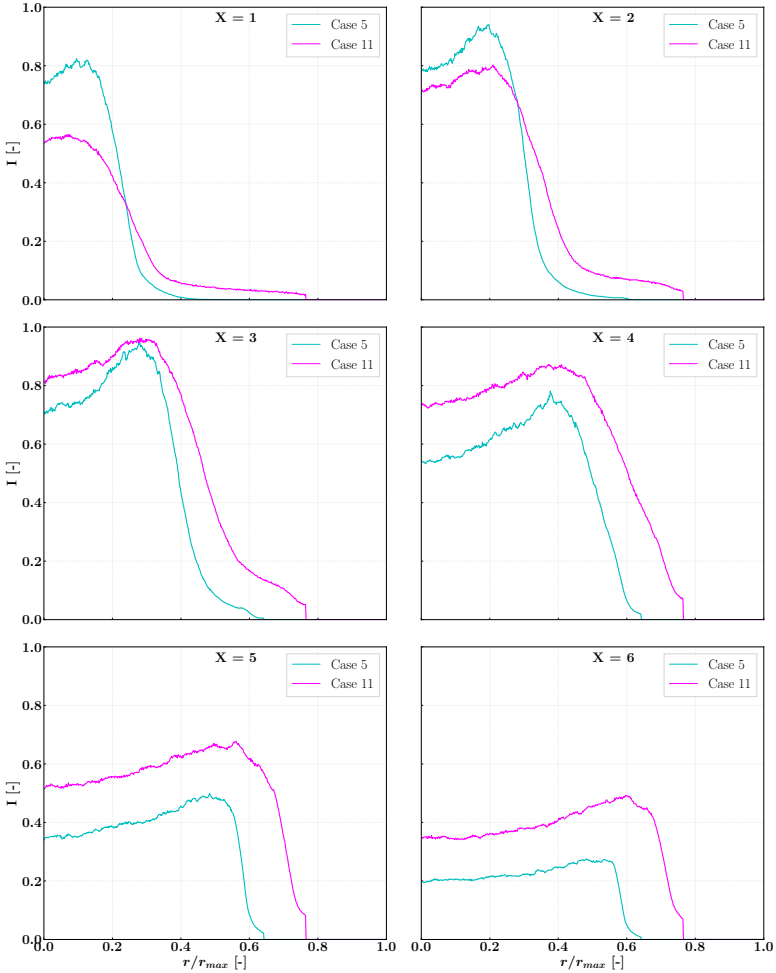

Figure 6.7: OH chemiluminescence intensity trends along the burner normalised radius at 6 equally spaced locations downstream the burner exit section for Case 5 and 11*

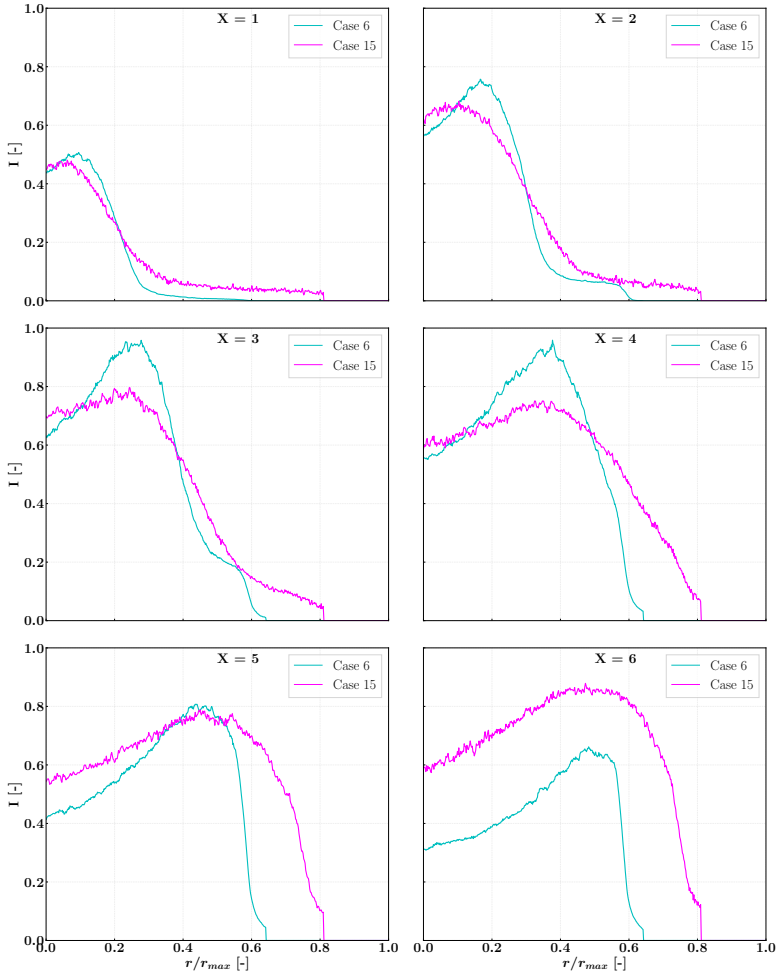

Figure 6.8: OH chemiluminescence intensity trends along the burner normalised radius at 6 equally spaced locations downstream the burner exit section for Case 6 and 15*

6.4 Emissions

Pollutant emissions were measured as well to assess the impact of CO_2 addition and the potential emission abatement linked to the application of EGR to gas turbine engines. Due to the limited availability of CO_2, only the two extreme fuel line split cases were tested, namely the 100% RF split and the 40% RF - 60% AF fuel split case. Indeed, for each test point a certain amount of time is required to reach steady state conditions for a correct emission sampling, limiting the number of tests that could be performed. In this case, data have been reported as the raw measured value and not corrected at 15% of O_2 at the exhaust, because the O_2 content of the inlet oxidant mixture is different for each case, and such comparison could lead to erroneous conclusions.

Figure 6.9 shows the CO emissions as a function of the oxygen molar concentration in the incoming mixture for the 100% RF fuel split (Case 7 to 9) ad the 40% RF - 60% AF fuel line split (Case 14 to 17). In a similar way, Figure 6.10 reports the NO_x emissions for the corresponding cases. In all cases, the measurements obtained in normal air conditions (21% oxygen molar fraction) are reported as well for a clearer comparison with the vicious air cases.

Starting from CO emissions, as the available oxygen diminishes the amount of CO in the exhaust increases. This is one of the main drawback of EGR and one of the main limitations in terms of EGR applicability apart from the flame stability. Indeed, the low availability of oxygen slows down the reactivity and the thermodynamic equilibrium shifts towards a higher CO production. The introduction of the axial fuel line helps to tackle this issue as long as the injected CO_2 amount is moderate. The CO rapidly increases in the 60% AF case at 19.5% oxygen molar concentration due to the lower oxidation rate.

An opposite trend can be found analysing NO_x emissions (Fig. 6.10). As pointed out also during the analysis of the OH radical distribution in Section 6.3, the CO_2 injection leads to a lower reactivity that in turns helps reducing NO_x emissions. This favourable effect is particularly evident at

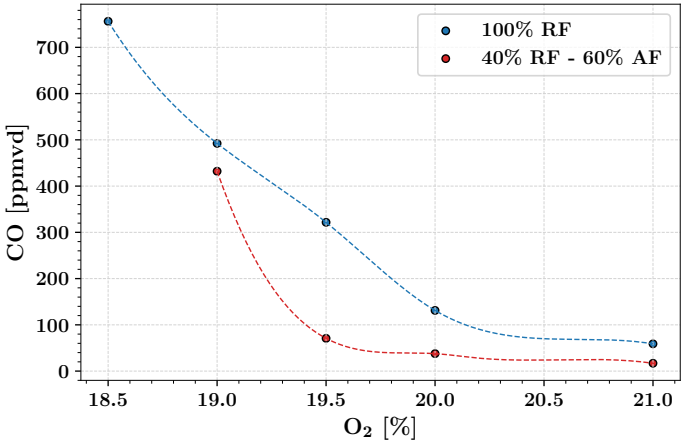

Figure 6.9: CO emissions as a function of the oxygen molar concentration for 100% RF and 40% RF - 60% AF fuel split case

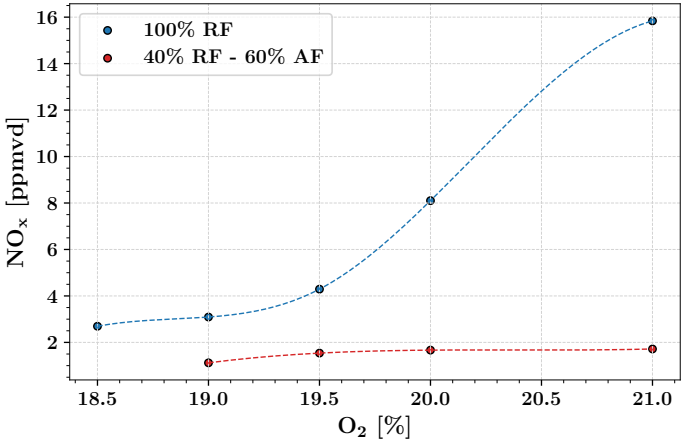

Figure 6.10: NO_x emissions as a function of the oxygen molar concentration for 100% RF and 40% RF - 60% AF fuel split case

100% RF where the NO_x emissions were found to be particularly high compared to the other tested splits because of the poorer mixing. For the 40% RF - 60% AF split case, the benefits in terms of NO_x emissions at decreasing oxygen availability are less evident. As pointed out in Section 5.3, the axial fuel line enhances the mixing and drives the NO_x abatement, overshadowing the effect related to the decrease in oxygen content.

Conclusions

The DLN combustion technology represents the state of the art gas turbine combustor systems to control the flame temperature and therefore pollutant emissions. Over recent years, several industries have explored the feasibility of integrating Exhaust Gas Recirculation with lean premixed combustion to tackle the emissions problem, while ensuring a stable combustion. However, the oxygen depletion negatively affects both the flame stability and CO emissions, representing the real limiting factors associated with EGR employment. Such a complex combustion process, regardless of the significant improvements in terms of reliability of computational models, requires dedicated experimental investigations throughout the entire design process. However, testing at close to engine conditions is extremely expensive, especially when optical diagnostics is involved.

For this purpose, this work starts with the design of a novel reactive atmospheric test rig capable of hosting real hardware components. The rig is specifically build to be easily adjusted to different burner concepts and to investigate the combustion process through optical diagnostics technique. Therefore, particular attention was paid to the design of the optical accesses to allow a proper flame visualisation.

In particular, the present work focuses on the characterisation of a novel lean premixed burner for industrial applications developed by Baker Hughes.

In the first part, the burner flow field is studied though PIV measurements. Experiments are performed both in non reactive and reactive

conditions to analyse the impact of the combustion process on the burner flow field. The typical recirculation zones of swirl stabilised flames are clearly identified, with minor modifications introduced by the flame development. The shear layer locations, responsible for the generation of the highly turbulent region to enhance the mixing, are identified allowing the definition of the flame anchoring area. As swirling flows are particularly known for their highly turbulent flow field, the burner is additionally studied from an unsteady point of view analysing the velocity fluctuations in terms of root mean square and turbulent kinetic energy.

The second part focuses on the flame investigation through OH* chemiluminescence measurements. The burner is tested at different adiabatic flame temperatures and in various fuel split configurations, to capture the effect of the axial fuel line on the flame behaviour not only in terms of shape and position but also from a pollutant emissions point of view. Indeed, when the solely radial line is fed, an increase in flame temperature causes a shift in the flame position: the higher jet penetration moves the flame stabilisation region further downstream the burner exit section and the flame assumes a lifted shape.

A similar behaviour is found in the analysis of the fuel split at constant flame temperature, where the fuel jet velocity of the radial line is found to affect the flame anchoring position: at high and low radial content the flame is lifted, while at more balanced splits the flame anchors in the recirculation zone inside the burner dump region. However, in terms of emissions, both CO and NO_x benefit from an increase in the axial line content as the flame reactivity lessens, as observed from the chemiluminescence maps. On the contrary, the burner stability limits worsen as the radial line content is decreased, being responsible for the flame stabilisation process.

In conclusion the axial fuel line globally enhance the mixing providing a more uniform fuel distribution, which is an important aspect in terms of pollutant emissions but simultaneously it is detrimental for the flame stability as richer regions are important for the flame stabilisation.

The burner is finally tested in vitiated air conditions, at increasing

CO_2 content. The same adiabatic flame temperature as in standard air conditions is targeted for a proper comparison. From the OH* maps, the rapid drop in chemiluminescence intensity is clearly visible as the oxygen content is decreased, indicating a lower flame reactivity. As expected, the burner performance in terms of stability worsen as the oxygen available for the combustion process decreases. In vitiated air conditions, the reaction process is globally delayed and the flame position shifts downstream while maintaining the same shape. However, at 40% RF - 60% AF fuel split, the combined effect of the axial fuel line increase and oxygen decrease leads to an abrupt change in the flame shape: the reaction zone is widespread involving almost the entire liner. A sudden change in the Da number could be one of the possible reasons behind such behaviour, as it represents the flow to chemical time scale ratio. Indeed, the OH radical distribution pointed out a marked increase in the reaction time scale as the CO_2 content grows.

In terms of emissions, one of the major drawback of air vitiation is the increase in CO emissions. As the oxidiser oxygen content decreases, the CO amount increases accordingly and a benefit from the 40% RF - 60% AF fuel split is still found. However, around 19% oxygen molar fraction, the amount of CO emissions of the aforementioned fuel split almost matches the 100%RF case. A similar behaviour is found when analysing the NO_x emissions trends. At the most favourable conditions in terms of NO_x emissions in standard air conditions, the potential emission abatement of close to EGR conditions is not really marked. On the contrary, the 100% RF case strongly benefit from an oxidiser oxygen decrease. Therefore, a fuel flow split more biased towards the radial line could help the flame stability while not leading to such an increase in terms of emissions.

Finally, the present study remarks the importance of dedicated experimental investigations to understand the flame behaviour and to have a better overview of new burner concept performance in terms of emissions and stability limits. Chemiluminescence, being relatively simple to implement, bares the potential for a flame diagnostics able to drive the burner design from the early phases of the design process. In addition, the large

amount of data collected throughout this work could be useful for the validation of numerical models, especially when analysing unstable phenomena like the lean blow out or non conventional conditions as CO_2-air oxidant mixtures.

To further address the flame stability issue, additional investigations could explore the possibility of adding localised hydrogen jets in the pilot region. In this way, higher EGR values could be achieved without compromising the combustion stability. Combustion diagnostics can provide a better understanding of the flame stabilisation mechanism supporting the CFD numerical modelling. Indeed, the combustion regimes coming from the separate injection of different fuel into a CO_2 vitiated oxidiser are particularly difficult to predict. Therefore, numerical models can certainly benefit from dedicated optical diagnostics experimental investigations, where both the OH and CH radical could give an insight on the different fuel distribution along with the flame position.

Bibliography

[1] IEA. World Energy Outlook 2022. Technical report, IEA, Paris, France, 2022. URL https://www.iea.org/reports/world-energy-outlook-2022.

[2] Khallaghi, Navid, Hanak, Dawid P., and Manovic, Vasilije. "Techno-economic evaluation of near-zero CO2 emission gas-fired power generation technologies: A review." *Journal of Natural Gas Science and Engineering*, 74:103095, feb 2020. ISSN 1875-5100. doi: 10.1016/J.JNGSE.2019.103095.

[3] Raffel, Markus, Willert, Christian E, Scarano, Fulvio, Kähler, Christian J, Wereley, Steven T, and Kompenhans, Jürgen. *Particle Image Velocimetry: A Practical Guide*. Springer International Publishing AG, third edit edition, 2018.

[4] Lauer, Martin and Sattelmayer, Thomas. "On the adequacy of chemiluminescence as a measure for heat release in turbulent flames with mixture gradients." *Journal of Engineering for Gas Turbines and Power*, 132(6):1–8, 2010. ISSN 15288919. doi: 10.1115/1.4000126.

[5] Luque, Jorge and Crosley, David R. "Transition probabilities and electronic transition moments of the A–X and D–X progressions systems of nitric oxide." *The Journal of Chemical Physics*, 111(16): 7405, oct 1999. ISSN 0021-9606. doi: 10.1063/1.480064. URL https://aip.scitation.org/doi/abs/10.1063/1.480064.

[6] Lieuwen, Tim, Chang, Michael, and Amato, Alberto. "Stationary gas turbine combustion: Technology needs and policy considerations." *Combustion and Flame*, 160(8):1311–1314, aug 2013. ISSN 0010-2180. doi: 10.1016/J.COMBUSTFLAME.2013.05.001.

[7] Shih, Wang Ping, Lee, Jong Guen, and Santavicca, Domenic A. "Stability and emissions characteristics of a lean premixed gas turbine combustor." *Symposium (International) on Combustion*, 26(2):2771–2778, jan 1996. ISSN 0082-0784. doi: 10.1016/S0082-0784(96)80115-9.

[8] Guethe, Felix, García, Marta De La Cruz, and Burdet, André. "Flue Gas Recirculation in Gas Turbine: Investigation of Combustion Reactivity and NOX Emission." *Proceedings of the ASME Turbo Expo*, 2:179–191, feb 2009. doi: 10.1115/GT2009-59221. URL `/GT/proceedings-abstract/GT2009/48838/179/344800`.

[9] Burdet, André, Lachaux, Thierry, De La Cruz García, Marta, and Winkler, Dieter. "Combustion Under Flue Gas Recirculation Conditions in a Gas Turbine Lean Premix Burner." *Proceedings of the ASME Turbo Expo*, 2(PARTS A AND B):1083–1091, dec 2010. doi: 10.1115/GT2010-23396. URL `/GT/proceedings-abstract/GT2010/43970/1083/339275`.

[10] Li, Hejie, ElKady, Ahmed M., and Evulet, Andrei T. "Effect of Exhaust gas recirculation on NOx formation in premixed combustion system." *47th AIAA Aerospace Sciences Meeting including the New Horizons Forum and Aerospace Exposition*, 2009. doi: 10.2514/6.2009-226. URL `https://arc.aiaa.org/doi/10.2514/6.2009-226`.

[11] Tanaka, Yusuke, Nose, Masakazu, Nakao, Mitsuhiro, Saitoh, Keijiro, Ito, Eisaku, and Tsukagoshi, Keizo. Development of Low NOx Combustion System with EGR for 1700°C-class Gas Turbine. Technical Report 1, Mitsubishi Heavy Industries, 2013.

[12] Burnes, Dan, Saxena, Priyank, and Dunn, Paul. "Study of Using Exhaust Gas Recirculation on a Gas Turbine for Carbon Capture."

Proceedings of the ASME Turbo Expo, 5, jan 2020. doi: 10.1115/GT2020-16080.

[13] ElKady, Ahmed M., Evulet, Andrei, Brand, Anthony, Ursin, Tord Peter, and Lynghjem, Arne. "Exhaust Gas Recirculation in DLN F-Class Gas Turbines for Post-Combustion CO2 Capture." *Proceedings of the ASME Turbo Expo*, 3(PART B):847–854, aug 2008. doi: 10.1115/GT2008-51152. URL `/GT/proceedings-abstract/GT2008/43130/847/328317`.

[14] Evulet, Andrei T., ELKady, Ahmed M., Branda, Anthony R., and Chinn, Daniel. "On the Performance and Operability of GE's Dry Low NOx Combustors utilizing Exhaust Gas Recirculation for Post-Combustion Carbon Capture." *Energy Procedia*, 1(1):3809–3816, feb 2009. ISSN 1876-6102. doi: 10.1016/J.EGYPRO.2009.02.182.

[15] Giorgetti, Simone, De Paepe, Ward, Bricteux, Laurent, Parente, Alessandro, and Contino, Francesco. "Carbon Capture on a Micro Gas Turbine: Assessment of the Performance." *Energy Procedia*, 105:4046–4052, may 2017. ISSN 1876-6102. doi: 10.1016/J.EGYPRO.2017.03.854.

[16] Petersen, Nils Hendrik, Bexten, Thomas, Goßrau, Christian, and Wirsum, Manfred. "Analysis of the Emission Reduction Potential and Combustion Stability Limits of a Hydrogen-Fired Gas Turbine With External Exhaust Gas Recirculation." *Proceedings of the ASME Turbo Expo*, 4, sep 2021. doi: 10.1115/GT2021-58674. URL `/GT/proceedings-abstract/GT2021/84966/1120009`.

[17] Park, Yeseul, Choi, Minsung, Kim, Dongmin, Lee, Joongsung, and Choi, Gyungmin. "Performance analysis of large-scale industrial gas turbine considering stable combustor operation using novel blended fuel." *Energy*, 236:121408, dec 2021. ISSN 0360-5442. doi: 10.1016/J.ENERGY.2021.121408.

[18] De Santis, Andrea, Ingham, Derek B., Ma, Lin, and Pourkashanian, Mohamed. "CFD analysis of exhaust gas recirculation in a micro gas turbine combustor for CO2 capture." *Fuel*, 173:146–154, jun 2016. ISSN 0016-2361. doi: 10.1016/J.FUEL.2016.01.063.

[19] Cameretti, Maria Cristina, Tuccillo, Raffaele, and Piazzesi, Renzo. "Study of an exhaust gas recirculation equipped micro gas turbine supplied with bio-fuels." *Applied Thermal Engineering*, 59(1-2):162–173, sep 2013. ISSN 1359-4311. doi: 10.1016/J.APPLTHERMALENG.2013.04.029.

[20] Zhang, Shiheng, Li, Yangyang, Wang, Shuqian, Zeng, Haibo, Liu, Jingping, Duan, Xiongbo, and Dong, Hao. "Experimental and numerical study the effect of EGR strategies on in-cylinder flow, combustion and emissions characteristics in a heavy-duty higher CR lean-burn NGSI engine coupled with detail combustion mechanism." *Fuel*, 276:118082, sep 2020. ISSN 0016-2361. doi: 10.1016/J.FUEL.2020.118082.

[21] Galindo, José, Climent, Héctor, Navarro, Roberto, and García-Olivas, Guillermo. "Assessment of the numerical and experimental methodology to predict EGR cylinder-to-cylinder dispersion and pollutant emissions." *International Journal of Engine Research*, 22(10):3128–3146, dec 2021. ISSN 20413149. doi: 10.1177/1468087420972544. URL `https://journals.sagepub.com/doi/abs/10.1177/1468087420972544`.

[22] Gicquel, L. Y.M., Staffelbach, G., and Poinsot, T. "Large Eddy Simulations of gaseous flames in gas turbine combustion chambers." *Progress in Energy and Combustion Science*, 38(6):782–817, dec 2012. ISSN 0360-1285. doi: 10.1016/J.PECS.2012.04.004.

[23] Hasti, Veeraraghava Raju, Lucht, Robert P., and Gore, Jay P. "Large eddy simulation of hydrogen piloted CH4/air premixed combustion with CO2 dilution." *Journal of the Energy Institute*, 93(3):1099–1109, jun 2019. ISSN 1743-9671. doi: 10.1016/J.JOEI.2019.10.004.

[24] Nassini, Pier Carlo, Pampaloni, Daniele, Meloni, Roberto, and Andreini, Antonio. "Lean blow-out prediction in an industrial gas turbine combustor through a LES-based CFD analysis." *Combustion and Flame*, 229:111391, jul 2021. ISSN 0010-2180. doi: 10.1016/J.COMBUSTFLAME.2021.02.037.

[25] Jaravel, T., Riber, E., Cuenot, B., and Bulat, G. "Large Eddy Simulation of an industrial gas turbine combustor using reduced chemistry with accurate pollutant prediction." *Proceedings of the Combustion Institute*, 36(3):3817–3825, jan 2017. ISSN 1540-7489. doi: 10.1016/J.PROCI.2016.07.027.

[26] Guethe, F., Guyot, D., Singla, G., Noiray, N., and Schuermans, B. "Chemiluminescence as diagnostic tool in the development of gas turbines." *Applied Physics B: Lasers and Optics*, 107(3):619–636, 2012. ISSN 09462171. doi: 10.1007/s00340-012-4984-y.

[27] Guethe, Felix, Stankovic, Dragan, Genin, Franklin, Syed, Khawar, and Winkler, Dieter. "Flue Gas Recirculation of the Alstom Sequential Gas Turbine Combustor Tested at High Pressure." *Proceedings of the ASME Turbo Expo*, 2(PARTS A AND B):399–408, may 2012. doi: 10.1115/GT2011-45379. URL `/GT/proceedings-abstract/GT2011/54624/399/357781`.

[28] Guyot, Daniel, Guethe, Felix, Schuermans, Bruno, Lacarelle, Arnaud, and Paschereit, Christian Oliver. CH*/OH* Chemiluminescence Response of an Atmospheric Premixed Flame Under Varying Operating Conditions, jun 2010. URL `https://doi.org/10.1115/GT2010-23135`.

[29] De Persis, Stéphanie, Cabot, Gilles, Pillier, Laure, Gökalp, Iskender, and Boukhalfa, Abdelakrim Mourad. "Study of lean premixed methane combustion with CO2 dilution under gas turbine conditions." *Energy and Fuels*, 27(2):1093–1103, 2013. ISSN 08870624. doi: 10.1021/ef3016365.

[30] Kline, S.J. and McClintock, F. A. "Describing Uncertainties in Single-Sample Experiments." *Mechanical Engineering*, 75:3–8, 1953.

[31] Lefebvre, Arthur H. and Ballal, Dilip R. "Gas Turbine Combustion : Alternative Fuels and Emissions, Third Edition." *Gas Turbine Combustion*, apr 2010. doi: 10.1201/9781420086058. URL https://www.taylorfrancis.com/books/mono/10.1201/9781420086058/gas-turbine-combustion-arthur-lefebvre-dilip-ballal.

[32] ASME Boiler and Pressure Vessel Committee on Pressure Vessels. *Asme Boiler and Pressure Vessel Code - VIII Division 1: Rules for Construction of Pressure Vessels*. ASME, New York, 2010.

[33] Cerutti, Matteo, Roma, Michele, Picchi, Alessio, Becchi, Riccardo, and Facchini, Bruno. "Improving Emission and Blow-Out Characteristics of Novel Natural Gas Low NOx Burners for Heavy Duty Gas Turbine." *Proceedings of the ASME Turbo Expo*, 4B-2019, nov 2019. doi: 10.1115/GT2019-91235.

[34] Cerutti, Matteo, Riccio, Giovanni, Andreini, Antonio, Becchi, Riccardo, Facchini, Bruno, and Picchi, Alessio. "Experimental and numerical investigations of novel natural gas low NOx burners for heavy duty gas turbine." *Journal of Engineering for Gas Turbines and Power*, 141(2), feb 2019. ISSN 15288919. doi: 10.1115/1.4040814/366411. URL https://asmedigitalcollection.asme.org/gasturbinespower/article/141/2/021006/366411/Experimental-and-Numerical-Investigations-of-Novel.

[35] Cerutti, Matteo, Nassini, Pier Carlo, Pampaloni, Daniele, and Andreini, Antonio. "Experimental and numerical characterization of a novel natural gas low NOx burner in gas turbine realistic environment." *Journal of Engineering for Gas Turbines and Power*, 143(7), jul 2021. ISSN 15288919. doi: 10.1115/1.4049446/1093906. URL https://asmedigitalcollection.asme.org/gasturbinespower/article/143/7/071018/1093906/Experimental-and-Numerical-Characterization-of-a.

[36] Tropea, C., Yarin, A., and Foss, J.F. *Springer Handbook of Experimental Fluid Mechanics*. Springer Berlin Heidelberg, 1 edition, 2007. doi: 10.1007/978-3-540-30299-5.

[37] Dantec Dynamics. *FlowManager software and Introduction to PIV Instrumentation*. 2000.

[38] Westerweel, J. "Fundamentals of digital particle image velocimetry." *Measurement Science and Technology*, 8(12):1379, dec 1997. ISSN 0957-0233. doi: 10.1088/0957-0233/8/12/002. URL `https://iopscience.iop.org/article/10.1088/0957-0233/8/12/002https://iopscience.iop.org/article/10.1088/0957-0233/8/12/002/meta`.

[39] He, Lei, Guo, Qinghua, Gong, Yan, Wang, Fuchen, and Yu, Guangsuo. "Investigation of OH* chemiluminescence and heat release in laminar methane–oxygen co-flow diffusion flames." *Combustion and Flame*, 201:12–22, 2019. ISSN 15562921. doi: 10.1016/j.combustflame.2018.12.009.

[40] Sardeshmukh, Swanand, Bedard, Michael, and Anderson, William. "The use of OH* and CH* as heat release markers in combustion dynamics." *International Journal of Spray and Combustion Dynamics*, 9(4):409–423, 2017. ISSN 17568285. doi: 10.1177/1756827717718483.

[41] Eckbreth, Alan C. *Laser Diagnostics for Combustion Temperature and Species*. CRC Press, second edi edition, jan 1996. ISBN 9781003077251. doi: 10.1201/9781003077251. URL `https://www.taylorfrancis.com/books/mono/10.1201/9781003077251/laser-diagnostics-combustion-temperature-species-alan-eckbreth`.

[42] Linne, Mark A. *Spectroscopic measurement : an introduction to the fundamentals*. Academic Press, 2002. ISBN 9780080517537.

[43] Hollas, J. Michael. *Modern spectroscopy*. John Wiley & Sons Ltd, fourth edi edition, 2004. ISBN 0 470 84415 9. doi: 10.1016/0022-2860(87)85092-5.

[44] Montgomery Smith, L., Keefer, Dennis R., and Sudharsanan, S. I. "Abel inversion using transform techniques." *Journal of Quantitative Spectroscopy and Radiative Transfer*, 39(5):367–373, may 1988. ISSN 0022-4073. doi: 10.1016/0022-4073(88)90101-X.

[45] Terhaar, Steffen, Krüger, Oliver, and Paschereit, Christian Oliver. "Flow Field and Flame Dynamics of Swirling Methane and Hydrogen Flames at Dry and Steam Diluted Conditions." *Journal of Engineering for Gas Turbines and Power*, 137(4), oct 2014. ISSN 0742-4795. doi: 10.1115/1.4028392. URL `https://doi.org/10.1115/1.4028392`.